Unsteady melting and solidification of a Nano-Encapsulated Phase Change Materials hybrid nanofluid in an eccentric porous annulus

Mohammad Ghalambaz[1*], S.A.M. Mehryan[2], Kasra Ayoubi Ayoubloo[3], Ahmad Hajjar[4],

Mohammad Saidul Islam[5], Obai Younis[6,7], Maryam Ghodrat[8]

[1] Department of Theoretical Mechanics, Tomsk State University, Tomsk, Russia

[2] Young Researchers and Elite Club, Yasooj Branch, Islamic Azad University, Yasooj, Iran.

[3] Department of Mechanical Engineering, Shahid Chamran University of Ahvaz, Ahvaz, Iran

[4] ECAM Lyon, LabECAM, Université de Lyon, Lyon, France

[5] School of Mechanical and Mechatronic Engineering, Faculty of Engineering and Information Technology, University of Technology Sydney, Ultimo, NSW 2007, Australia

[6] Department of Mechanical Engineering, College of Engineering in Wadi Addwasir, Prince Sattam Bin Abdulaziz University, Al- Kharj, Saudi Arabia.

[7] Department of Mechanical Engineering, Faculty of Engineering, University of Khartoum, Sudan

[8] School of Engineering and Information Technology, University of New South Wales Canberra, Canberra 2610 ACT, Australia. Email: m.ghodrat@unsw.edu.au

*Corresponding author: Mohammad Ghalambaz (m.ghalambaz@gmail.com).

Abstract

A detailed knowledge of the melting and solidification of a suspension of Nano-Encapsulated Phase Change Materials (NEPCM) is essential to analyze the thermal behavior of the PCM materials. This study investigates the convective heat analysis of NEPCM suspensions during the solidification and melting process in a porous domain. The inner cylinder of the eccentric annulus is used as a thermally active wall for charging and discharging the suspension while an adiabatic condition is used at the outer wall of the cylinder. The thermal behavior of the suspension comprising nano-encapsulated PCM is analyzed throughout the melting and solidification process. The PCM core fusion temperature and eccentricity of the annulus affect the thermal performance. The overall heat transmission decreases when the PCM core fusion heat approaches to the suspension temperature. An increase in thermal convection between the nanofluid and porous matrix reduces the Nusselt number in the liquid but increases the heat transmission in the porous foam. An increase in Stefan number enhances the heat transfer in the enclosure.

1. Introduction

The energy consumption is increasing with the industrialization and Energy Information Administration (EIA) predicts a 50% rise in the overall energy uses by 2050 [1]. petroleum and other liquids (200 quadrillions Btu), coal (about 210 quadrillions Btu), natural gas (about 140 quadrillion Btu) is significantly higher than renewable energy (about 100 quadrillions Btu) [1]. The increasing use of natural energy resources is the leading mechanism of climate change and global warming, and it is expected a rise of global warming ranges from 1.1°C to 6.4°C by 21st century [2]. The limited resources of natural energy and its negative impacts on the environment influence the researcher to think about a more sustainable energy system, which is renewable solar energy. EIA predicts a 3.1% increase of the renewable energy consumption per year from 2018 to 2050, while 2.1% increase from other sources (0.6% petroleum, 0.4% coal and 1.1% natural gas) [1, 2]. However, renewable solar energy is not always available, and the key challenge is to develop an effective and efficient thermal management system.

Scientists over the last few decades applied different approches to store the thermal energy in various systems [3-5]. The latent energy storage technique is found more efficient and effective for solid-liquid transition due to its phase-change ability, small volume, and compactness [6]. The thermos-physical properties of the Phase Change Material (PCM) make heat storing system more efficient than other storage systems. However, the solidification and melting method of the latent heat process is reported low due to the lower thermal conductivity of the PCM materials [7]. A wide range of studies have used different techniques to enhance the heat transfer process of PCM [8-10]. Nano-encapsulation technique is reported efficient for the thermal management during the melting and solidification of the PCM materials [11].

Dispersing PCM nanoparticles, NEPCM, in a liquid is a novel approach to rise the heat capacity of a working fluid [12]. A few numbers of studies analyzed the melting and solidification process for PCM dispersed in a liquid and reported the thermal behavior of the working liquids [13-15]. However, many recent publications addressed the heat transfer of nanofluids [16-18] in enclosures. The similarity between NEPCM-suspensions and nanofluids is both are liquids containing stabilized nanoparticles. In nanofluids, the nanoparticles are always in the solid phase and do not undergo a phase transition, while the NEPCM particles in a NEPCM suspension can undergo a phase transition and absorb latent heat. A buoyancy-driven numerical approach investigated the thermal performance of a NEPCM suspension and investigated the contours of phase change in an enclosure [15]. Sheikholeslami et al. [19] investigated the convective heat transfer of magnetic nanofluids in a porous domain. Their results showed that the heat conduction model and shape of nanoparticles are the key controlling parameters. An analytical study employed a cylindrical enclosure and analyzed the melting and solidification process during volumetric heat generation [20]. The study analyzed the melting time variation for different radiuses of the cylindrical enclosure during heat generation and reported that the thermal storage ability is higher for positive and negative heat generation. An experimental study synthesized the nano-encapsulated PCM (palmitic acid and SiO_2) via the sol-gel approach and analyzed the solidification and melting process [21].

The heat transfer of the water-nano-encapsulated PCM was examined in a square computational domain. The left wall of the domain was exposed to a transient oscillating temperature. The study reported that a greater heat of the PCM core enhances the thermal performance of the system. A Lattice Boltzmann based study analyzed the convective melting process of nano-encapsulated PCM in a semicircular domain and reports that a higher volume of

the nanoparticle increases the thermal ability of the PCM [22]. Double diffusive heat transfer of NEPCM suspensions was examined in an astroid-shaped cavity [14]. The results showed that the Stefan number could effectively influence the heat transfer in the enclosure.

The cylinder enclosures are of great importance in industrial and domestic applications such as solar collectors, chemical reactors, and thermal energy storage units. The cylindrical enclosures were investigated for typical liquids and nanofluids in some recent studies [16, 23, 24].

The cylindrical annulus enclosures provide an excellent geometry for thermal energy storage since the working fluid can flow in the inner annuli and charge or discharge the enclosure. Moreover, the presence of a metal foam provides an extended surface that could enhance the charging/discharging of NEPCM particles through the interaction between the suspension and the porous matrix. Thus, the current geometry filled by a metal foam is an excellent choice for thermal energy storage applications. Since, an important aspect of using NEPCM suspensions is the un-steady heat transfer and energy storage effect of the phase change particles, the present study aims to investigate the un-steady phase change energy storage and heat transportation of NEPCM-suspension in an annulus field packed with a porous medium for the first time. Due to the high thermal conductivity of metal foams, the local thermal non-equilibrium effects, using the two-heat equation model, were taken into account.

2. Problem physics

2.1 Physical model

A 2-D porous annulus is saturated with a water-NEPCM suspension. The problem physics is demonstrated in Fig. 1. As indicated in Figs. 1 (a) and (b), heated (T_h) or cooled (T_c) condition is

used at the location (0, e) for the inner cylinder. However, the outer wall is subject to zero heat flux. The suspension temperature initially can adopt T_c or T_h upon the inner surface temperature. Hence, it is clear that the particle's core undergoes phase change. The radius ratio of the system is r_o/r_i. The core and shell of the particles are respectively nonadecane and polyurethane (PU). Aluminum foam is used for the solid matrix of the porous system. The local thermal non-equilibrium (LTNE) condition is assumed to be established. The solid matrix and suspension comprising components properties are provided in Table 1. The latent heat of the NEPCMs core is 211 kJ/kg and the phase change temperature is 32 °C [25]. Due to the symmetry of the model a half of the enclosure was selected as the computational domain, which is depicted in Fig. 1(c). Excluding the density in the momentum source, the characteristics of the liquid are considered to be constant. The impact of the buoyancy phenomenon is applied through the Boussinesq approximation.

2.2. The model formulation

The equations demonstrating thermal and hydrodynamic behavior of the laminar suspension have been listed below:

$$\frac{\partial u}{\partial x} + \frac{\partial v}{\partial y} = 0 \tag{1}$$

$$\frac{\rho_{nf}}{\varepsilon}\frac{\partial u}{\partial t} + \frac{\rho_{nf}}{\varepsilon^2}\left(u\frac{\partial u}{\partial x} + v\frac{\partial u}{\partial y}\right) = -\frac{\partial p}{\partial x} + \frac{\mu_{nf}}{\varepsilon}\left(\frac{\partial^2 u}{\partial x^2} + \frac{\partial^2 u}{\partial y^2}\right) - \frac{\mu_{nf}}{\kappa}u \tag{2a}$$

$$\frac{\rho_{nf}}{\varepsilon}\frac{\partial v}{\partial t} + \frac{\rho_{nf}}{\varepsilon^2}\left(u\frac{\partial v}{\partial x} + v\frac{\partial v}{\partial y}\right) = -\frac{\partial p}{\partial y} + \frac{\mu_{nf}}{\varepsilon}\left(\frac{\partial^2 v}{\partial x^2} + \frac{\partial^2 v}{\partial y^2}\right) + g\,\rho_{nf}\,\beta_{nf}\left(T_{nf} - T_c\right) - \frac{\mu_{nf}}{\kappa}v \tag{2b}$$

6

$$\varepsilon\left(\rho C_p\right)_{nf}\frac{\partial T_{nf}}{\partial t}+\left(\rho C_p\right)_{nf}\left(u\frac{\partial T_{nf}}{\partial x}+v\frac{\partial T_{nf}}{\partial y}\right)=\varepsilon k_{nf}\left(\frac{\partial^2 T_{nf}}{\partial x^2}+\frac{\partial^2 T_{nf}}{\partial y^2}\right)+h\left(T_s-T_{nf}\right) \quad (3a)$$

$$(1-\varepsilon)\left(\rho C_p\right)_s\frac{\partial T_s}{\partial t}=(1-\varepsilon)k_s\left(\frac{\partial^2 T_s}{\partial x^2}+\frac{\partial^2 T_s}{\partial y^2}\right)-h\left(T_s-T_{nf}\right) \quad (3b)$$

It is worth noting that the heat capacity term in Eq. (3a) contains a temperature dependent term representing the phase change of nanoparticles which is introduced in the next section. Moreover, *nf* and *s* of the above equations refer to the nanofluid and the solid matrix, respectively.

The boundary conditions are:

At active wall: $\forall$ *x, y, t* $\left|\begin{array}{l} x^2+(y-e)^2=r_i^2, t\geq 0 \Rightarrow u=v=0, \\ \textit{Heat charge of NEPCM particles}: T_{nf}=T_s=T_h \\ \textit{Heat discharge of NEPCM particles}: T_{nf}=T_s=T_c \end{array}\right.$ (4-a)

At adiabatic wall: $\forall$ *x, y, t* $\left| x^2+y^2=r_o^2, t\geq 0 \Rightarrow u=v=0, \dfrac{\partial T_{nf}}{\partial n}=\dfrac{\partial T_s}{\partial n}=0\right.$ (4-b)

Symmetry line: $\forall$ *y, t* $\left| x=0, u=0, \dfrac{\partial T_{nf}}{\partial x}=\dfrac{\partial T_s}{\partial x}=0\right.$ (4-c)

Also, the initial condition is as follows:

Initial condition $\forall$ *x, y, t* $\left|\begin{array}{l} r_i^2<x^2+(y-e)^2<r_o^2, t=0 \Rightarrow u=v=0, \\ \textit{Heat charge of NEPCM particles}: T_{nf}=T_s=T_c \\ \textit{Heat discharge of NEPCM particles}: T_{nf}=T_s=T_h \end{array}\right.$ (4-d)

2.3. Suspension properties

The suspension's density is evaluated as a weighted function of the base fluid and NEPCM particles [26]:

$$\rho_b = (1-\phi)\rho_f + \phi\rho_p \tag{5}$$

The f and p subscripts indicate the base fluid and the particles, respectively. The particle's density is assessed as [27]:

$$\rho_p = \frac{(1+\iota)\rho_c \rho_{sh}}{\rho_{sh} + \iota\rho_c} \tag{6}$$

Here is the density and subscripts of sh and c are the shell and particles' core, respectively. The symbol $\iota \sim 0.447$ [25] shows the ι is the core to the shell weight ratio. The specific heat capacity of the suspension can be calculated as [28, 29]:

$$C_{p,b} = \frac{(1-\phi)\rho_f C_{p,f} + \phi\rho_p C_{p,eff,p}}{\rho_b} \tag{7}$$

In the absence of the phase change, $C_{p,eff,p}$ represent the particles sensible heat capacity, and $C_{p,p}$: [27]:

$$C_{p,p} = \frac{(C_{p,c} + \iota C_{p,sh})\rho_c \rho_{sh}}{(\rho_{sh} + \iota\rho_c)\rho_p} \tag{8}$$

The latent heat of change phase could be taken into account as a part of the particles' sensible heat capacity [26, 30]:

$$C_{p,eff,p} = C_{p,p} + \left\{ \frac{\pi}{2} \cdot \left(\frac{h_{sf}}{T_{Mr}} - C_{p,p} \right) \cdot \sin\left(\pi \frac{T_{nf} - T_{fu} + T_{Mr}/2}{T_{Mr}} \right) \right\} \gamma$$

$$\gamma = \begin{cases} 0 & T_{nf} < T_{fu} - T_{Mr}/2 \\ 1 & T_{fu} - T_{Mr}/2 < T_{nf} < T_{fu} + T_{Mr}/2 \\ 0 & T_{nf} > T_{fu} + T_{Mr}/2 \end{cases} \tag{10}$$

The volumetric thermal-expansion coefficient for the suspension is evaluated as [29]:

$$\beta_b = \phi\beta_p + (1-\phi)\beta_f \tag{11}$$

2.4 Normalized governing equations

To normalize the equations and the corresponding boundary conditions, the transforming variations are utilized:

$$X = \frac{x}{L}, \ Y = \frac{y}{L}, R_i = \frac{r_i}{L}, R_o = \frac{r_o}{L}, \ E_c = \frac{e}{L}, \ U = \frac{uL}{\alpha_f}$$

$$V = \frac{vL}{\alpha_f}, \ P = \frac{pL^2}{\rho_f \alpha_f^2}, \ \theta_{nf} = \frac{T_{nf} - T_c}{\Delta T}, \ \theta_s = \frac{T_s - T_c}{\Delta T}, \ \tau = \frac{\alpha_f t}{L^2} \tag{13}$$

in which, $L = r_o - r_i$ and $\Delta T = T_h - T_c$. Hence, we then have:

$$\frac{\partial U}{\partial X} + \frac{\partial V}{\partial Y} = 0 \tag{16}$$

$$\varepsilon^{-2}\rho_r\left(\varepsilon\frac{\partial U}{\partial \tau} + U\frac{\partial U}{\partial X} + V\frac{\partial U}{\partial Y}\right) = -\frac{\partial P}{\partial X} + Pr\,\varepsilon^{-1}\mu_r\left(\frac{\partial^2 U}{\partial X^2} + \frac{\partial^2 U}{\partial Y^2}\right) - \frac{Pr}{Da}\mu_r u \tag{17}$$

$$\varepsilon^{-2}\rho_r\left(\varepsilon\frac{\partial V}{\partial \tau} + U\frac{\partial V}{\partial X} + V\frac{\partial V}{\partial Y}\right) = -\frac{\partial P}{\partial Y} + Pr\,\varepsilon^{-1}\mu_r\left(\frac{\partial^2 V}{\partial X^2} + \frac{\partial^2 V}{\partial Y^2}\right)$$

$$+ Ra \cdot Pr\,\beta_r\rho_r\theta - \frac{Pr}{Da}\mu_r v \tag{18}$$

The parameters in the transformed equations (17) and (18), Rayleigh number *Ra*, Prandtl number *Pr*, and Darcy number *Da*, respectively, are:

$$Ra = \frac{g\,\rho_{bf}\,\beta_{bf}\,\Delta T L^3}{\alpha_{bf}\,\mu_{bf}}, \ Pr = \frac{\mu_{bf}}{\rho_{bf}\,\alpha_{bf}}, \ Da = \frac{K}{L^2} \tag{19}$$

Also,

$$\mu_r = \left(\frac{\mu_{nf}}{\mu_{bf}}\right), \; \rho_r = \left(\frac{\rho_b}{\rho_f}\right) = (1-\phi) + \phi\left(\frac{\rho_p}{\rho_f}\right), \beta_r = \left(\frac{\beta_b}{\beta_f}\right) = (1-\phi) + \phi\left(\frac{\beta_p}{\beta_f}\right) \qquad (20)$$

It is assumed that the particles and host share a same thermal expansion coefficient, and accordingly, $\beta_r \sim 1$.

$$Cr\left(\varepsilon\frac{\partial\theta}{\partial\tau} + U\frac{\partial\theta_{nf}}{\partial X} + V\frac{\partial\theta_{nf}}{\partial Y}\right) = \varepsilon k_r\left(\frac{\partial^2\theta_{nf}}{\partial X^2} + \frac{\partial^2\theta_{nf}}{\partial Y^2}\right) + H\left(\theta_s - \theta_{nf}\right) \qquad (21)$$

where

$$k_r = \left(\frac{k_{nf}}{k_{bf}}\right), \; Cr = \frac{(\rho C_p)_{nf}}{(\rho C_p)_{bf}} = (1-\phi) + \phi\lambda + \frac{\phi}{\delta \, Ste}f \qquad (22)$$

The term $H(\theta_s\text{-}\theta_{nf})$ indicates the heat transfer between the solid porous medium and the NEPCM suspension inside the pores. Following Barlak et al. [25], $k_r = 1.24$ and μ_r=1.5 can be estimated. Here, Cr denotes the ratio of the heat capacity of the suspension to the sensible heat capacity of the liquid. The following non-dimensional parameters

$$\delta = \frac{T_{Mr}}{\Delta T}, \; \lambda = \frac{\left(C_{p,c} + \iota C_{p,sh}\right)\rho_c\rho_{sh}}{(\rho C_p)_{bf}\left(\rho_{sh} + \iota\rho_c\right)}, \; Ste = \frac{(\rho C_p)_{bf}\Delta T\left(\rho_{sh} + \iota\rho_c\right)}{h_{sf}\rho_c\rho_{sh}} \qquad (23)$$

indicate the non-dimensional melting interval (δ), sensible heat capacity ratio (λ), and Stefan number Ste. The Stefan number compares the temperature-difference times heat capacity (apparent heat) to the latent heat of fusion. Thus, a large value of Stefan's number indicates the latent heat of fusion is not significant compared to the sensible heat. In the present study, the Stefan number is smaller than unity, indicating the importance of the latent heat of particles. The dimensionless phase change function, f, is defined as:

$$f = \frac{\pi}{2}\sin\left(\frac{\pi}{\delta}(\theta - \theta_f + \delta/2)\right) \times \begin{cases} 0 & \theta < \theta_f - \delta/2 \\ 1 & \theta_f - \delta/2 < \theta < \theta_f + \delta/2 \\ 0 & \theta > \theta_f + \delta/2 \end{cases} \tag{24}$$

Here, θ_{fu} is the non-dimensional fusion temperature:

$$\theta_{fu} = \frac{T_{fu} - T_c}{T_h - T_c} \tag{25}$$

The energy balance equation for the solid matrix in the dimensionless form is achieved as:

$$(1-\varepsilon)\frac{(\rho C_p)_s}{(\rho C_p)_{bf}}\frac{\partial \theta_s}{\partial \tau} = (1-\varepsilon)K_{r,s}\left(\frac{\partial^2 \theta_s}{\partial X^2} + \frac{\partial^2 \theta_s}{\partial Y^2}\right) - H(\theta_s - \theta_{nf}) \tag{26}$$

where

$$K_{r,s} = \frac{k_s}{k_{bf}}, \quad H = \frac{hL^2}{k_{bf}} \tag{27}$$

According to the data presented in Table 1, $K_{r,s} = 334.42$. Eventually, the transformed conditions were achieved:

At active wall: $\forall X, Y, \tau$ $\left|\begin{array}{l} X^2 + (Y - E_c)^2 = R_i^2, \tau \geq 0 \Rightarrow U = V = 0, \\ \begin{cases} Heat\ charge\ of\ NEPCM\ particles: \theta_{nf} = \theta_s = 1 \\ Heat\ discharge\ of\ NEPCM\ particles: \theta_{nf} = \theta_s = 0 \end{cases} \end{array}\right.$ (24-a)

At adiabatic wall: $\forall X, Y, \tau$ $\left| X^2 + Y^2 = R_o^2, \tau \geq 0 \Rightarrow U = V = 0, \frac{\partial \theta_{nf}}{\partial n} = \frac{\partial \theta_s}{\partial n} = 0 \right.$ (24-b)

Symmetry line: $\forall Y, \tau$ $\left| X = 0, \tau \geq 0 \Rightarrow U = 0, \frac{\partial \theta_{nf}}{\partial X} = \frac{\partial \theta_s}{\partial X} = 0 \right.$ (24-c)

Initial condition $\quad \forall\ X,\ Y, \tau$ $\left|\begin{array}{l} R_i^2 < X^2 + \left(Y - E_c\right)^2 < R_o^2,\ \tau = 0 \Rightarrow U = V = 0, \\ \left\{\begin{array}{l} \text{Heat charge of NEPCM particles} : \theta_{nf} = \theta_s = 0 \\ \text{Heat discharge of NEPCM particles} : \theta_{nf} = \theta_s = 1 \end{array}\right. \end{array}\right.$ (24-d)

Considering the initial condition presented in Eq. (24-d), the nanoparticles are super cold in the case of heat charging and superheat in the case of discharging conditions. The initial concentration of nanoparticles is also controlled by the parameter ϕ specified in the caption of figures in the results section.

The Nusselt numbers on the inner circular wall are evaluated as:

$$Nu_{nf,l} = k_{r,nf}\left(\frac{\partial \theta_{nf}}{\partial n}\right)_{X^2 + \left(Y - E_c\right)^2 = R_i^2} \qquad (25\text{-}a)$$

$$Nu_{s,l} = K_{r,s}\left(\frac{\partial \theta_s}{\partial n}\right)_{X^2 + \left(Y - E_c\right)^2 = R_i^2} \qquad (25\text{-}b)$$

The Nusselt numbers averaged over the walls are determined as:

$$Nu_{nf} = \frac{1}{\pi}\int_0^\pi Nu_{nf,l}\,d\omega \qquad (26\text{-}a)$$

$$Nu_s = \frac{1}{\pi}\int_0^\pi Nu_{s,l}\,d\omega \qquad (26\text{-}b)$$

The overall heat transfer, Q_t , is also evaluated as:

$$Q_t = Nu_{nf} \times \varepsilon + Nu_s \times \left(1 - \varepsilon\right) \qquad (27)$$

The time-averaged heat transfer rates can be defined as follows:

$$Nu_{nf,a} = \frac{1}{\tau_{max}} \int_0^{\tau_{max}} Nu_{nf} d\tau \qquad (28\text{-}a)$$

$$Nu_{s,a} = \frac{1}{\tau_{max}} \int_0^{\tau_{max}} Nu_s d\tau \qquad (28\text{-}b)$$

$$Q_{t,a} = \frac{1}{\tau_{max}} \int_0^{\tau_{max}} Q_t d\tau \qquad (28\text{-}c)$$

The streamlines were also introduced in the usual way.

3. Numerical approach, mesh check, and verifications

3.1. Numerical method

The governing equations and the boundary conditions were implemented in COMSOL (Ver. 5.4) software and integrated by means of the Finite Element Method (FEM). User-defined functions implemented the phase change equations. The quadratic Lagrange shape functions were used for the heat and momentum equations. The heat equations and momentum equations were treated as fully coupled. Then, the Newton method, with a damping factor of 0.9, was employed to numerically solve the corresponding algebraic equations with a relative error of 0.005. This relative error provides only a 0.5% error in computations, which is acceptable for most engineering applications and graphical representations of the results. The following specifications were employed in the model and solver to obtain an accurate converged solution. Cr term and f were introduced by user-defined functions as variable terms. The stream function for computation of streamlines was defined using nojac function to isolate its impact on the governing equations during a multi-physics coupled process. Dirichlet boundary condition of zero streamline value at

the boundary conditions was employed in the streamline function. The backward differentiation formula was used for automatic time step control. The Jacobian update was set to once per time step; the maximum number of iterations for each time step was 25 with a tolerance factor of 0.5 and memory allocation factor of 1.2.

3.2. Mesh test

Here a non-uniform quad mesh was utilized to discretize the domain of the solution. The accuracy of the obtained solution was tested by repeating the computations for several mesh sizes. The meshes were dense next to the walls and stretched toward the core region of the cavity with an element ratio of 10. The constructed mesh with a size of 100×100 is exhibited in Fig. 2. The critical case of the highest Rayleigh number and Darcy number was selected as the mesh study. Table 2 shows the specifications of selected meshes and the corresponding computational times. The computations were performed for the following set of non-dimensional parameters $Ste = 0.2$, $Da = 10^{-4}$, $R_r = 2.5$, $\lambda = 0.32$, $E_c = -0.75$, $H = 100$, $\varepsilon = 0.95$, $\theta_{fu} = 0.5$, $\phi = 0.04$, $Pr = 6.2$, $k_r = 1.24$, $\mu_r = 1.5$, and $Ra = 10^7$. The computed results for average Nusselt numbers of the suspension phase and porous matrix are plotted in Fig. 3. As seen, the results for various mesh sizes are almost identical. The key parameter of the present model is the phase change of nanoparticles in the enclosure. Hence, the impact of mesh size on the phase change region was investigated in Fig. 4 for two non-dimensional time steps of $\tau=0.007$ and $\tau=0.03$. As seen in Figs. 4(a)-(c), the phase change region of $\tau=0.007$ cannot be captured with the coarse meshes of I-III, and there are some discontinuities. These observed discontinuities are due to the poor resolution of coarse meshes, which cannot properly explore the narrow phase change regions. Fig. 4(d) depicts no discontinuity in phase change regions, and hence, its corresponding mesh, i.e., Case IV, due to better mesh quality than other cases, could be adequate for computations. Thus, by considering the outcomes

14

of Table 2, Figs. 3 and 4, the mesh of Case IV was selected for computations with acceptable accuracy and reasonable computational costs.

3.3. Verifications

By making comparisons to theoretically and experimentally studies in the field, the validity of the simulations was verified. The localized heating transfer was compared to a research by Baaytas and Pop [31] for a pure fluid with no nanoparticles. The localized heating transfer was compared to a research by Baytas and Pop [31] for same instance as shown in Fig. 5, and there was a great deal of consistency. The study of Baytas and Pop was a non-dimensional study for a range of potential temperatures and working fluids. Thus, the computations were executed for the same conditions as [31]. As depicted in Table 3, the heat transfer of nanofluids was also compared with the study of Kahveci [32] for the natural convection of water containing nanoparticles in a clear square cavity with no phase change. The Nusselt number was computed for the case of $Ra =$ 1E6, $Pr =$0.62E1, $Nv = 2.88$, and $Nc = 3.3$. These values of Nc and Nv are corresponding to Brinkman and Maxwell models of dynamic viscosity and thermal conductivity of the study of Kahveci [32] for selected nanoparticles. The average Nusselt number for 5% of alumina nanoparticles was obtained as 9.78, while in the present study, it was computed as 9.77. The transient heat transfer rate was compared with the study of Kalabin et al. [33], and found in very good agreement (Fig. 6). Kalabin et al. [33] numerically studied the transient natural convection flow in an inclined square domain with time-sinusoidal temperature. Finally, the natural convection heat transfer in an annulus enclosure was compared with the experimental study of Kuehn and Goldestein [34] for a clear fluid. As can be seen from Fig. 7, the computed temperature patterns are very close to the measured ones.

15

4. Results and discussion

The goal of the current study is to analyze the fundamental thermo hydrodynamic behavior of the NEPCM-suspension in an eccentric annulus. Taking into account the reported findings of Barlak et al. [25], the suspension to base fluid's thermal conductivity ratio could be estimated as 1.24 when $\phi = 0.04$. Also, the dynamic viscosity's ratio is 1.5 for the same concentration. Moreover, the sensible heat capacity ratio was chosen as λ=0.32 [25], the radii ratio, $R_r = 2.5$, Rayleigh number, $Ra = 10^7$, Darcy number $Da = 10^{-4}$ are considered to be fixed. The simulations were commenced for the alterable parameters of the Stefan number $0.2 < Ste < 1$, non-dimensional fusion temperature $0.05 \leq \theta_{fu} \leq 0.95$, interfacial heat transfer coefficient, $1 \leq H \leq 100000$, eccentricity $-0.75 \leq E_c \leq 0.75$, the volume concentration of NEPCM particles $\phi = 0.0$ and 4%, and porosity, $\varepsilon = 0.95$ and 0.97.5.

4.1. Melting heat transfer

First, the thermal and flow behaviors are studied when the inner cylinder is heated and the NEPCM core is undergoing a melting process. The outlines of the heat capacity ratio Cr and the streamlines in the cavity are depicted in Fig. 8 at different instants. As the Cr contours shows, the domain is divided into two regions. One is in the colored ribbon, and the other is out of that. Out of the ribbon, Cr is the sensible heat capacity of the nanofluid to that of the base fluid, and in the colored ribbon, Cr is the effective heat capacity, including the latent and sensible heat, to the sensible heat capacity of the base fluid. 0.97 refers to the value of Cr out of the colored ribbon in which the core of the nano-encapsulated phase change material is fully melted or completely in the solid phase.

The fluid surrounding the inner hot cylinder absorbs the heat and moves up due to the buoyancy effect while the cold fluid travels to bottom, and a circulating convective flow occurs.

16

This results in a recirculation zone covering the whole cavity with a concentration of the streamlines near the inner cylinder.

It can be seen that, initially, the flow intensifies due to the pressure difference between the hot and cold zones of the fluid, then the intensity of the flow diminishes when most of the fluid is heated, and the temperature is becoming uniform. Additionally, it should be noted that the red zones in the Cr contours correspond to the zone in which the NEPCM core undergoes melting. It is shown that as time goes by, the melting zone moves from the inner cylinder towards the outer one before finally vanishing. In fact, the PCM core melts when the surrounding temperature is close to the fusion temperature θ_{fu}. In this figure, $\theta_{fu} = 0.5$. As the fluid is progressively heating in the cavity, its temperature is increasing from 0 to 1, and the zone corresponding to θ_{fu} is shifting according to the temperature of the fluid. Finally, when the temperature of the fluid in the whole cavity increases higher than θ_{fu}, all the NEPCM core is melted, and the phase change ceases.

In addition to the Cr contours, Fig. 8 shows the streamlines in the cavity. It can be seen that a recirculation cell covers the whole cavity, indicating that a convective flow is taking place. In fact, the fluid in the vicinity of the hot cylinder is heated and undergoes a decrease in density, resulting in circulation in the upper direction. The cold fluid above then circulates downwards, gets heated, and goes upwards again. This circulation cycle leads to the recirculation cell observed in the enclosure. It is also noted that the intensity of the flow initially increases when the discrepancy between the hot and cold fluids is at its highest. This intensity then decreases after the fluid mixing and goes towards thermal equilibrium.

Fig. 9 shows the isothermal contours of the NEPCM suspension T_{nf} and of the solid matrix T_s at different instants. It is clear that the temperature increases progressively in the fluid and in the solid matrix, as indicated by the stratified isotherms, which are originally compacted close to the

inner cylinder as the heat source, then shifting away. The isotherms of T_{nf} and T_s corresponding to low temperatures disappear with time as most of the fluid is heated. Nonetheless, it can be seen that at the same position in the cavity, T_{nf} is lower than T_s, indicating that the heat is being transmitted faster in the metal foam than in the suspension, and thermal non-equilibrium is achieved. Indeed, when the NEPCM core melts, it absorbs heat without raising its temperature, which contributes to the thermal non-equilibrium among the solid matrix and fluid phase, mainly in the phase change region.

The temporal variation of the Nusselt numbers Nu_{nf} and Nu_s is plotted in Fig. 10 for different values of the fusion temperature of the NEPCM core θ_{fu}. It is clear that both Nu_{nf} and Nu_s are initially at their maximum where the heat transfer is very active, then decrease substantially with time as the fluid in the cavity is heated, and the temperature difference in the cavity is diminishing. The effect of θ_{fu} on the two Nusselt numbers seems inconsiderable, as Nu_s slightly rises with the increase of θ_{fu}, while Nu_{nf} is minimum when θ_{fu} is close to 1 and 0, i.e., the maximum and minimum temperatures at the inner and outer cylinders respectively, and shows a small increase when θ_{fu} is between 0.35 and 0.65. This is due to the fact that when the temperature is close to the hot cylinder temperature, the phase change will be limited to the region surrounding the inner cylinder, and its involvement in the total heat transfer will be limited. Moreover, when θ_{fu} is very low, the time of phase change will be limited as melting stops once the fluid's temperature in the whole enclosure exceeds θ_{fu}.

The temporal effect of the eccentricity E_c on the variation of Nu_{nf} and Nu_s is depicted in Fig. 11. Nu_{nf} is minimum for $E_c = 0.75$ while it is slightly higher for E_c=0 (concentric cylinders) and for $E_c = -0.75$. In fact, when E_c<0, the inner hot cylinder is located at the bottom, which intensifies the free convection where the hot fluid rises upwards, and the cold one falls downwards. On the

other hand, Nu_s is initially at its highest for $E_c = 0$, but later, it reaches a maximum value for $E_c = 0.75$ when convective heat transfer diminishes.

The temporal variation of Nu_{nf} and Nu_s is shown in Fig. 12 for selected values of the interfacial heat transfer coefficient H. In both cases, the effect of H is almost the same when its value is increased above 20000. Nonetheless, the effect of H on the two Nusselt numbers is different. While reducing H increases substantially the value of Nu_{nf} over the melting period, Nu_s does not show the same trend of variation. This is related to the temperature distribution in the cavity, as seen in the isothermal contours. As the temperature of the solid matrix is higher than that of the fluid, increasing H raises the part of heat transmitted from the solid phase towards the fluid. The part of the heat transmitted at the inner wall to the fluid from the overall heat transfer is thus reduced and Nu_{nf} decreased. Nu_s is very low for $H = 1$, but a significant rise is observed when H is increased above 100. Nu_s is maximum for the highest values of H when in the initial period ($\tau < 0.04$), and for $H = 100$ when $\tau > 0.04$.

Fig. 13 illustrates the influence of Stefan number Ste on the variation of Nu_{nf} and Nu_s as functions of time. It is clear that both of Nu_{nf} and Nu_s are slightly higher when Ste is decreased. A lower value of Ste corresponds to a rise in the NEPCM's latent heat, consequently, a larger involvement of the nanoparticles in the total heat transfer, which translates into an increase in the Nusselt numbers.

The impact of Rayleigh number on Nu_{nf} and Nu_s as functions of time is visualized in Fig. 14. The rise of the Ra surges the Nu_{nf}. Indeed, when Ra is increased, the buoyancy forces overcome the viscous ones and enhances the convection effects. A similar behavior can be seen for Nu_s. Nonetheless, this behavior depends on time. For $Ra = 10^7$, Nu_s is maximum when $\tau < 0.06$, but it becomes minimum when $\tau > 0.06$, where the free convection is inhibited.

Table 4 summarizes the effects of various considered parameters on the average Nusselt numbers Nu_{nf} and Nu_s and on the total heat transfer $Q_{t,a}$. It can be seen that for a porosity $\varepsilon = 0.95$, $Nu_{nf,a}$ is higher when a higher concentration of the NEPCM particles ϕ is used, but the opposite occurs for $\varepsilon = 0.975$. On the other hand, $Nu_{s,a}$ rises substantially when the porosity is increased but decreases with the rise of ϕ when the two cylinders are not concentric. Finally, it can be seen that the total heat transfer $Q_{t,a}$ is reduced when ϕ is raised, and when ε is decreased.

4.2. Solidification heat transfer

In this section, the flow and heat transfer inside the annulus are considered when the inner cylinder is cooled down and the NEPCM is solidifying.

Fig. 15 illustrates the Cr contours and the streamlines in the cavity at different instants. A recirculation covers the cavity owing to the temperature gradient in the suspension near the inner cold cylinder and the heated suspension away from the wall. The size of the recirculation zone and the intensity of this convective flow decrease with time as the fluid in the enclosure cools, and the temperature difference is reduced. Due to the reduction in the fluid temperature, which first occurs near the inner cylinder and then transmits into the whole cavity, the zone at which the PCM core solidifies shifts away from the inner cylinder toward the cavity center. As for the Cr contours, it is shown that the zone at which the NEPCM core undergoes solidification shifts upwards with time. As the fluid cools down, its temperature starts to decrease starting from the region in the vicinity of the inner cylinder, which explains the upward shift in solidification of the PCM.

The isothermal contours of T_{nf} and of T_s at different instants are depicted in Fig. 16. It can be seen that the contours were initially compacted near the inner cylinder, then became stratified,

indicating that the temperature decrease in the fluid is gradual. In addition, the temperature of the solid matrix is lower than that of the fluid. The PCM core solidifies at a constant temperature, so heat is being released without temperature variation, while the heat is being transmitted in the solid matrix without similar retardation. The solid matrix cools thus faster than the fluid, and a thermal non-equilibrium occurs. This thermal non-equilibrium is explained by the fact that when the core of the NEPCM undergoes solidification, it absorbs heat while remaining at a constant temperature. This effect is not present in the solid matrix, which absorbs heat in the form of sensible heat, which results in a faster drop in temperature compared to the NEPCM.

The variation of Nu_{nf} and Nu_s as functions of time is visualized in Fig. 17 for various θ_{fu}. It can be seen that Nu_{nf} is slightly higher for $\theta_{fu} = 0.35$ than for $\theta_{fu} = 0.65$ compared to the other values, while it is minimum for $\theta_{fu}=0.95$. On the other hand, Nu_s grows with the rise of θ_{fu} and reaches its maximum for $\theta_{fu}=0.95$, i.e., when θ_{fu} is almost equal to the maximum temperature. Nevertheless, the effect of θ_{fu} on the two Nusselt numbers remains limited. This is because the NEPCM core undergoes solidification in all cases. However, it is more limited when the fusion temperature is very high or very low, as the time of the phase change process is relatively low compared to other cases.

Fig. 18 depicts the variation of Nu_{nf} and Nu_s as functions of time for selected values of E_c. It is shown that Nu_{nf} is minimum for E_c=-0.75, as the inner cold cylinder is located at the bottom. In fact, the convective effects are increased when the cylinder is at the top. As the hot fluid goes up and the cold one goes down, raising the location of the cylinder enhances this effect by adding further cooling to the fluid in the upper region. Nonetheless, the effect of E_c on Nu_{nf} is not very significant. A similar trend can be seen for Nu_s for $\tau < 0.05$, where Nu_s is at its lowest value for

E_c=-0.75, but the opposite occurs when Nu_s becomes maximum for that value of E_c once the intensity of convection starts decreasing.

The temporal impact of H on the variation of Nu_{nf} and Nu_s is illustrated in Fig. 19. Raising H increases Nu_s but reduces Nu_{nf}. This is due to the fact that the solid matrix is colder than the fluid phase and so the fluid loses more heat towards the solid matrix when H is increased. The overall contribution of the heat transmitted from the fluid towards the inner cold cylinder is then reduced, and Nu_{nf} decreases. In addition, a considerable change in the two Nusselt numbers is observed when H is decreased to 1, while almost no effect can be seen when H is increased from 5000 to 10000.

The variation of Nu_{nf} and Nu_s as functions of time is plotted in Fig. 20 for selected values of Ste. Both Nu_{nf} and Nu_s decrease as Ste grows. As mentioned earlier, a reduction on the latent heat of the particle cores reduces the aid of NEPCMs to the overall transferred heat, and, as a consequence, the Nusselt numbers are reduced. Therefore, when the value of Ste is reduced, the NEPCM's latent heat is increased, which results in a higher contribution of the NEPCM to the overall heat transfer, leading to a rise in the values of Nusselt number.

Fig. 21 illustrates the influence of Ra on Nu_{nf} and Nu_s as functions of time. Increasing Ra raises the value of Nu_{nf}, and this rise is significant for $Ra = 10^7$ when the convective effects are very important. On the contrary, Nu_s decreases with Ra and is minimum for $Ra = 10^7$. In all cases, the slope of variation of Nusselt number is initially very high, then decreases with time. Indeed, the heat transfer is most active in the first stage, where the temperature difference in the cavity is at its highest, and the convective effects are maximized. As soon as the convective flow takes place, the temperature difference inside the enclosure is reduced, which diminishes the convective effects and consequently the heat transfer. This results in the change of the slope of Nu as observed.

The effects of various parameters on $Nu_{nf,a}$, $Nu_{s,a}$ and $Q_{t,a}$ are summarized in Table 5. Increasing ϕ from 0 to 0.04 raises $Nu_{nf,a}$ and $Nu_{s,a}$ for all the values of the other parameters. Similarly, both $Nu_{nf,a}$ and $Nu_{s,a}$ rise as porosity growth, which is due to the decline of the dynamic resistance of the solid matrix and intensification of the free convection. However, it is clear that Nu_s is several orders of magnitude greater than Nu_{nf}, which leads to a decrease in $Q_{t,a}$ when ε is raised, for the contribution of the heat transfer in the solid matrix will be lower according to equation (30). In addition, $Q_{t,a}$ increases for a higher value of ϕ. Of course, for a higher value of ϕ, more NEPCM particles are included and contribute to the heat transfer enhancement.

5. Conclusion

The thermal performance and energy storage of NEPCM hybrid nanofluids were modeled and explored in a porous annulus enclosure. The two-energy equation model, one equation for the heat transfer in the suspension and one equation for the heat transfer in the porous matrix, was used to model the thermal behavior of the hybrid nanofluid and the porous medium. The phase change NEPCM-particles suspended in the host fluid was modeled as a temperature-dependent variable heat capacity. The impact of using NEPCM particles on the stored/released energy and the heat transfer was discussed in detail. The following conclusions can be drawn from the present study:

- The fusion temperature θ_{fu} of the NEPCM core moves the region of phase change inside the cavity, as melting and solidification occur when the surrounding temperature is close to θ_{fu}. Heat transfer in the suspension is thus affected by θ_{fu}. The heat transfer is lower when θ_{fu} is very close to the temperature of the inner cylinder or to the initial temperature of the suspension.

- Changing the location of the inner cylinder by varying the eccentricity E_c affects the mechanism of the free convection in the cavity. In the case of melting (hot inner cylinder),

heat transfer is diminished when $E_c > 0$, i.e., when the inner cylinder is displaced toward the top. On the other hand, heat transfer is improved when $E_c > 0$ in the case of solidification.

- Reducing the interfacial heat transfer coefficient H enhances heat transfer in the fluid suspension and inhibits it in the solid matrix. This is due to the local thermal non-equilibrium and the temperature difference between the two phases leading to interfacial heat transfer between the two phases. In addition, increasing H above a certain limit (5000 in the current study) seems to have no additional effect on thermal behavior.

- Using a lower value of Stefan number, *Ste*, indicates a larger latent heat of the NEPCM core, and as a result, it leads to a higher participation of the NEPCMs in the overall heat transfer, which is finally translated by heat transfer enhancement.

Data statement:

All data are included in the manuscript.

List of tables

Table 1 Thermophysical specification of the utilized material [25]

Material	μ (kg/m. s)	β (K^{-1})	C$_p$ (J/Kg.K)	k (W/m.K)	ρ (Kg/m^3)
Host fluid	8.9×10^{-4}	21×10^{-5}	4179	0.613	997.1
PU	---	17.28×10^{-5}	1317.7	---	786
Nonadecane	---	---	2037	---	721
Solid matrix	—	—	897	205	2700

Table 2 Grid check detail

Cases	Case I	Case II	Case III	Case IV*	Case V	Case VI
Size of cases	100×100	150×150	200×200	**250×250**	300×300	400×400
Run time	20min 1s	43min 19s	81min 14s	**178min 3s**	540min 50s	874min 23s

* is the selected mesh size for computation of the results section.

Table 3 The average Nusselt number obtained in the present study and those reported by Kahveci [32]

ϕ	0	0.05	0.1
Kahveci [32]	9.23	9.783	10.297
Current investigation	9.20	9.76	10.3

25

Table 4 Impact of the dimensionless variables on Nu_{nf} and Nu_s for melting state when $Da = 10^{-4}$, $Rr = 2.5$, $\lambda = 0.32$, $H = 5000$, $\theta_{fu} = 0.5$, $Pr = 6.2$, $Ste = 0.5$, and $Ra = 10^7$

Variables		ϕ					
		0.00			0.04		
ε	E_c	$Nu_{nf,a}$	$Nu_{s,a}$	$Q_{t,a}$	$Nu_{nf,a}$	$Nu_{s,a}$	$Q_{t,a}$
0.95	-0.75	1.3638	126.53	7.6220	1.8979	74.743	1.9341
	0.00	1.3794	142.04	8.4123	1.6355	147.79	2.9430
	0.75	1.3512	120.94	7.3308	1.6143	69.760	1.6695
0.975	-0.75	2.7904	266.21	8.4009	1.3937	225.55	4.2798
	0.00	3.0303	272.36	9.0136	2.1753	291.46	5.4074
	0.75	2.6229	200.82	7.5778	1.2464	190.08	3.2443

Table 5 Influence of the particles concentration, porosity, and the cylinder location on Nu_{nf} and Nu_s for solidification state when $R_r = 2.5$, $\lambda = 0.32$, $H = 5000$, $\theta_{fu} = 0.5$, $Pr = 6.2$, $Da = 10^{-4}$, $Ste = 0.5$, and $Ra = 10^7$

Variables		ϕ					
		0.00			0.04		
ε	E_c	$Nu_{nf,a}$	$Nu_{s,a}$	$Q_{t,a}$	$Nu_{nf,a}$	$Nu_{s,a}$	$Q_{t,a}$
0.95	-0.75	1.2934	155.82	9.0197	1.5364	168.00	9.8594
	0.00	1.3217	161.28	9.3198	2.7127	172.25	10.239
	0.75	1.2658	157.96	9.1293	1.5230	172.36	10.065
0.975	-0.75	1.6146	261.53	8.1126	1.8631	281.52	8.8544
	0.00	1.7592	302.82	9.2856	2.1072	325.96	10.204
	0.75	1.7975	277.06	8.6791	1.9979	315.25	9.8293
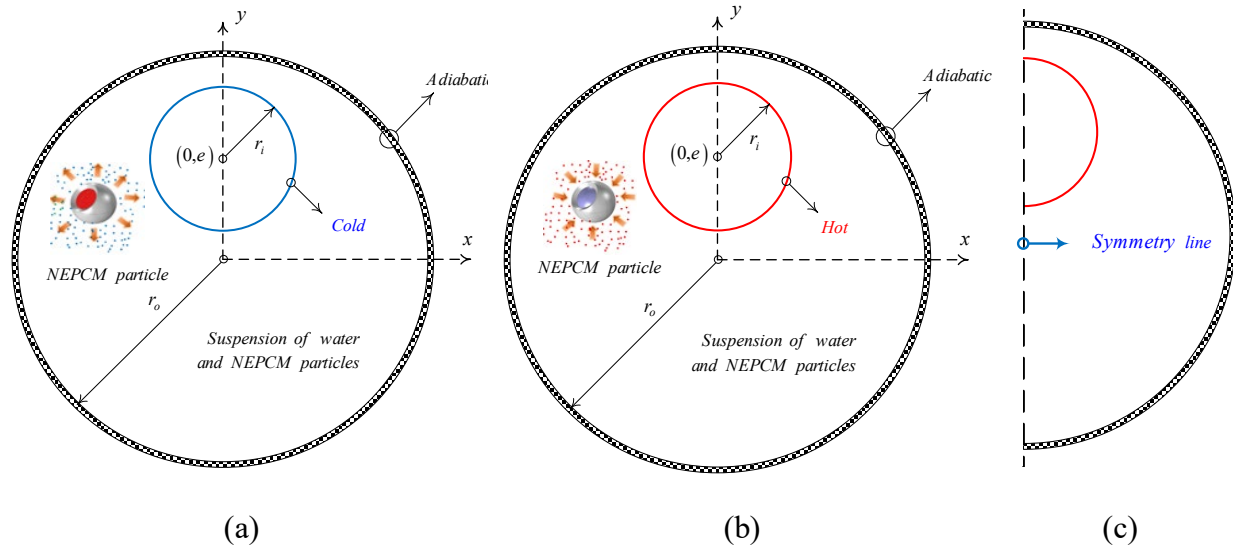
Fig. 1 Physical model and geometry details for NEPCM particles at (a): heat discharge, (b): heat charge states, and (c): computational domain
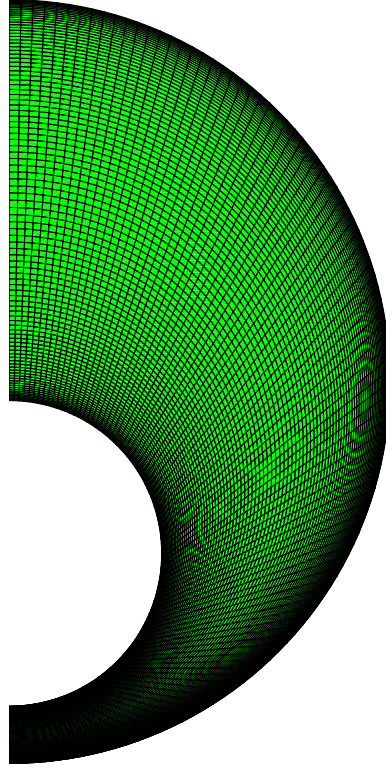
Fig. 2 Schematic of the constructed mesh size of 100×100.

(a)

(b)
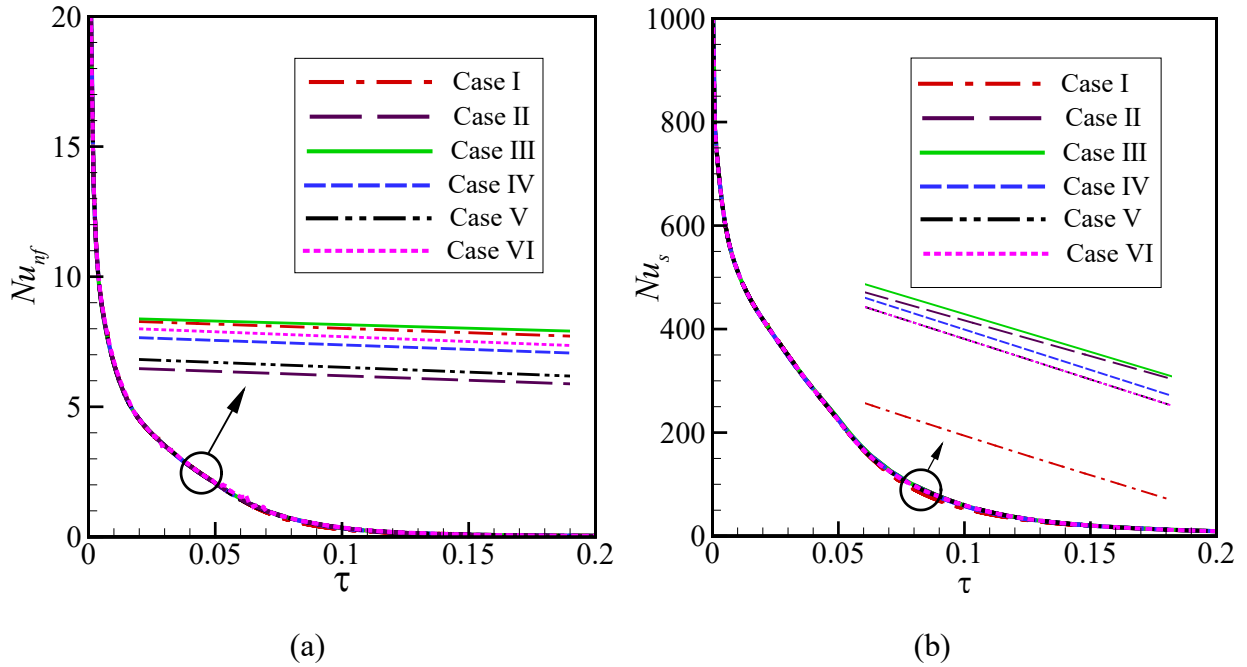
Fig. 3. The variation of (a) Nu_{nf} and (b) Nu_s for various cases of grid size when $Pr = 6.2$, $Ste = 0.2$, $R_r = 2.5$, $\lambda = 0.32$, $E_c = -0.75$, $H = 100$, $\varepsilon = 0.95$, $\theta_{fu} = 0.5$, $\phi = 0.04$, $Da = 10^{-4}$ and $Ra = 10^7$
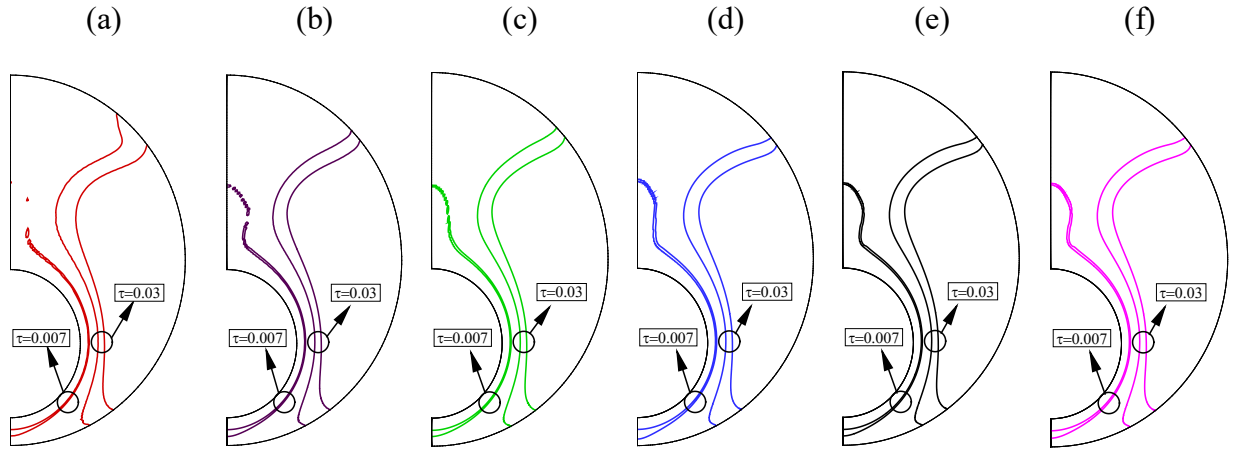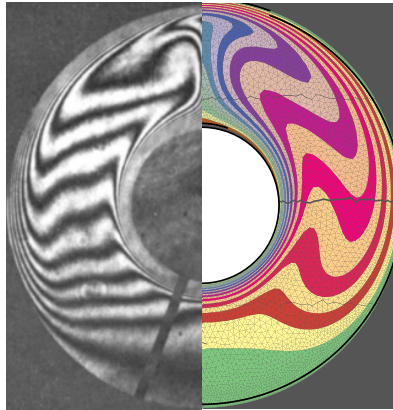
**Fig. 4.** Heat capacity ratio for various values of (a) Case I, (b) Case II, (c) Case III, (d) Case IV, (e) Case V and (f) Case VI in specific non-dimensional times $\tau = 0.007$ and $\tau = 0.03$ when $Pr = 6.2$, $Da = 10^{-4}$, $R_r = 2.5$, $\lambda = 0.32$, $E_c = -0.75$, $H = 100$, $\varepsilon = 0.95$, $\theta_{fu} = 0.5$, $\phi = 0.04$, $Ste = 0.2$, and $Ra = 10^7$
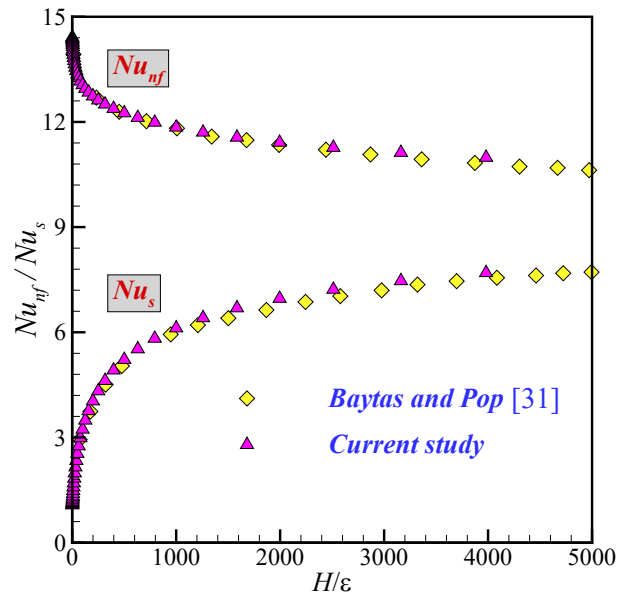

Fig. 5. The results of the present work and represented in [31]
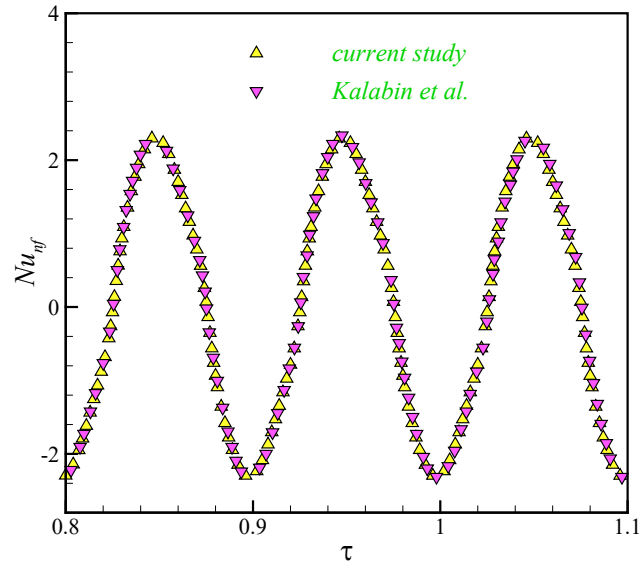
Fig. 6. Transient Nusselt numbers of the study conducted by Kalabin et al. [35] and present

work

Fig. 7 The temperature distribution in an annulus cavity computed in the present study (left) and the experimental measurement of [34] (right) when $Ec = 0$, $\phi=0$, $Ra = 2.33E5$, $Pr = 0.706$.
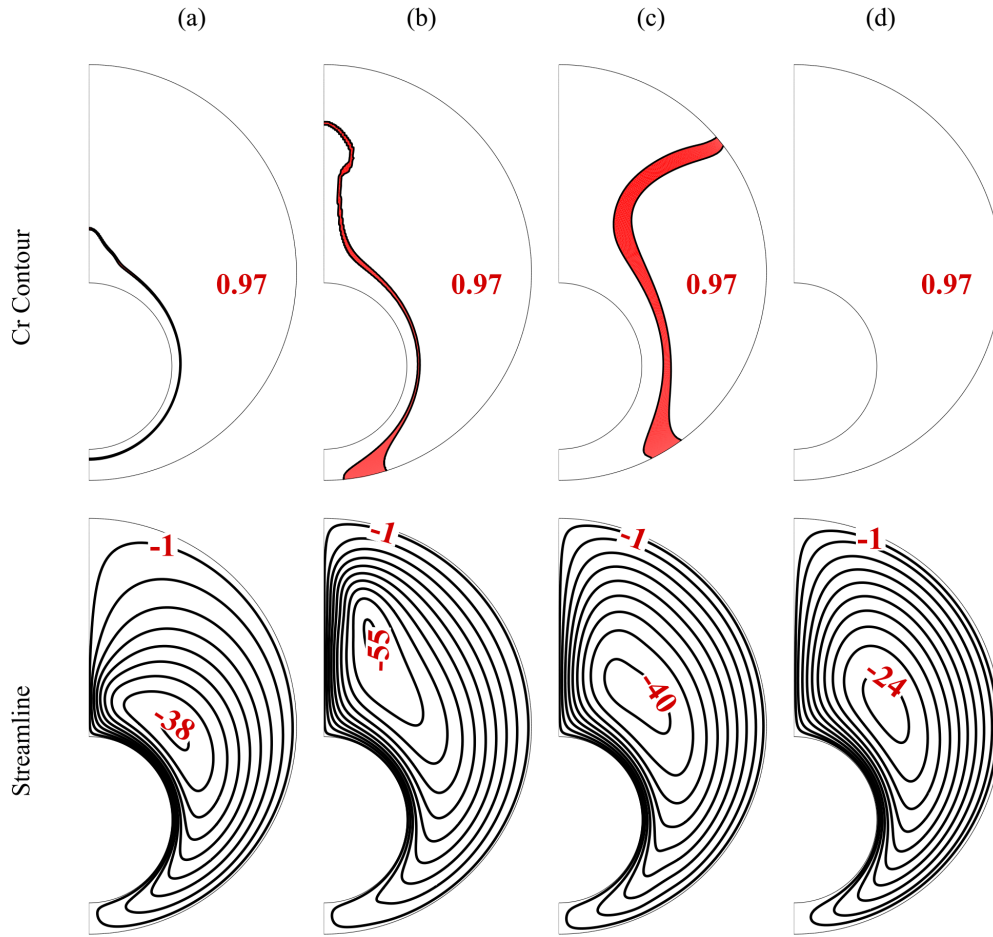
Fig. 8. The snapshots of heat capacity ratio contour and streamlines for melting state on (a) $\tau = 0.005$, (b) $\tau = 0.01$, (c) $\tau = 0.03$ and (d) $\tau = 0.06$ when $Da = 10^{-4}$, $R_r = 2.5$, $\lambda = 0.32$, , $Ste = 0.2$, $E_c = -0.75$, $H = 100$, $\varepsilon = 0.95$, $\theta_{fu} = 0.5$, $\phi = 0.04$, $Pr = 6.2$ and $Ra = 10^7$
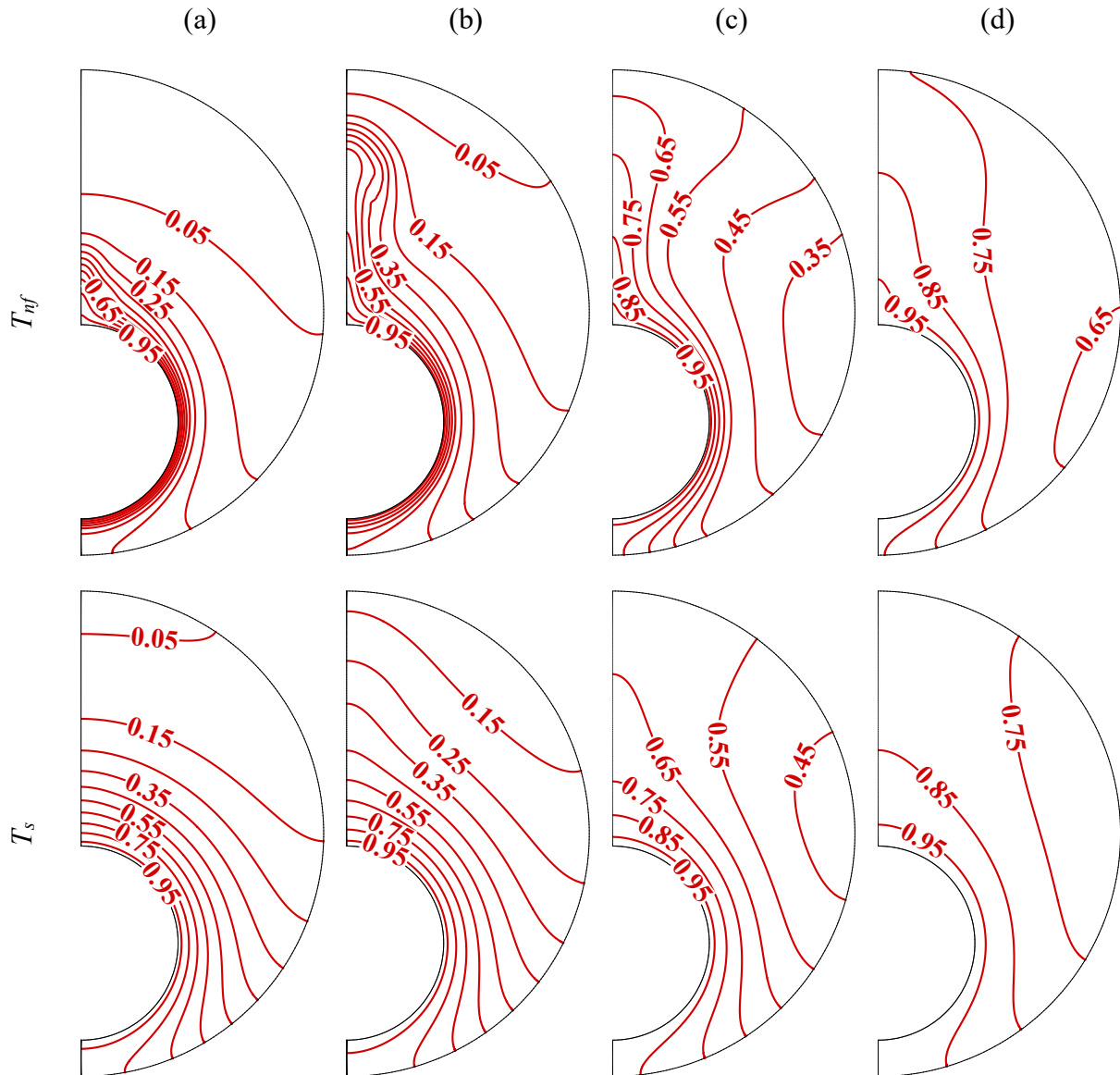
Fig. 9. The Temperature contour of T_{nf} and T_s during times for melting state on (a) $\tau = 0.005$, (b) $\tau = 0.01$, (c) $\tau = 0.03$ and (d) $\tau = 0.06$ when $Da = 10^{-4}$, $R_r = 2.5$, $\lambda = 0.32$, $E_c = -0.75$, $H = 100$, $\varepsilon = 0.95$, $\theta_{fu} = 0.5$, $\phi = 0.04$, $Ste = 0.2$, $Pr = 6.2$, and $Ra = 10^7$
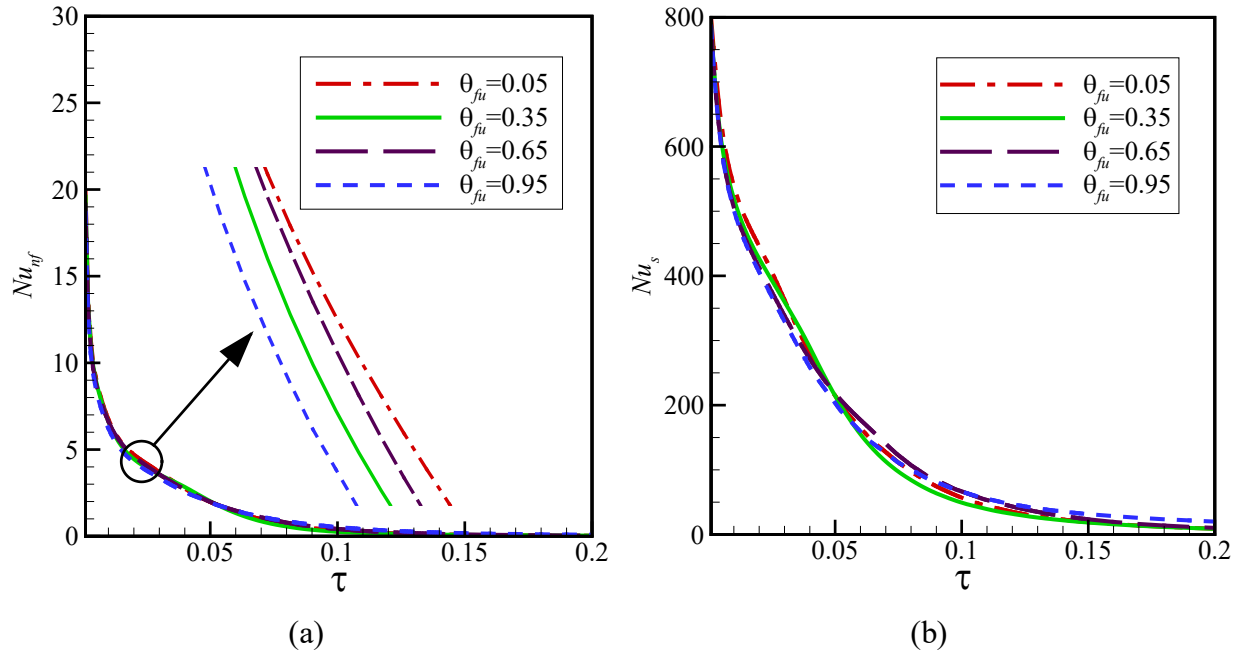
Fig. 10. The temporal various dimensionless fusion temperature for melting state on (a) Nu_{nf} (b) Nu_s when $Da = 10^{-4}$, $R_r = 2.5$, $\lambda = 0.32$, $E_c = -0.75$, $H = 100$, $\varepsilon = 0.95$, $\phi = 0.04$, $Ste = 0.5$, $Pr = 6.2$, and $Ra = 10^7$
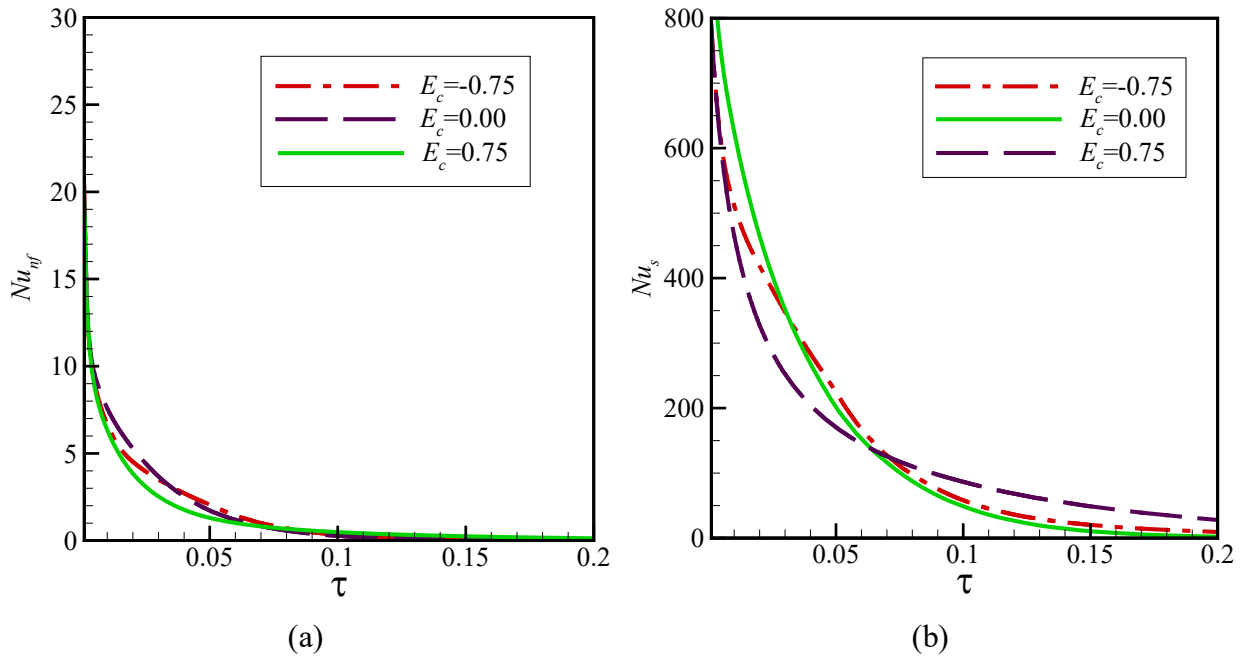
Fig. 11. The effect of various values of eccentricity for melting state on (a) Nu_{nf} (b) Nu_s during non-dimensional time when $Da = 10^{-4}$, $R_r = 2.5$, $\lambda = 0.32$, $H = 100$, $\varepsilon = 0.95$, $\theta_{fu} = 0.5$, $\phi = 0.04$, $Ste = 0.5$, $Pr = 6.2$, and $Ra = 10^7$

33
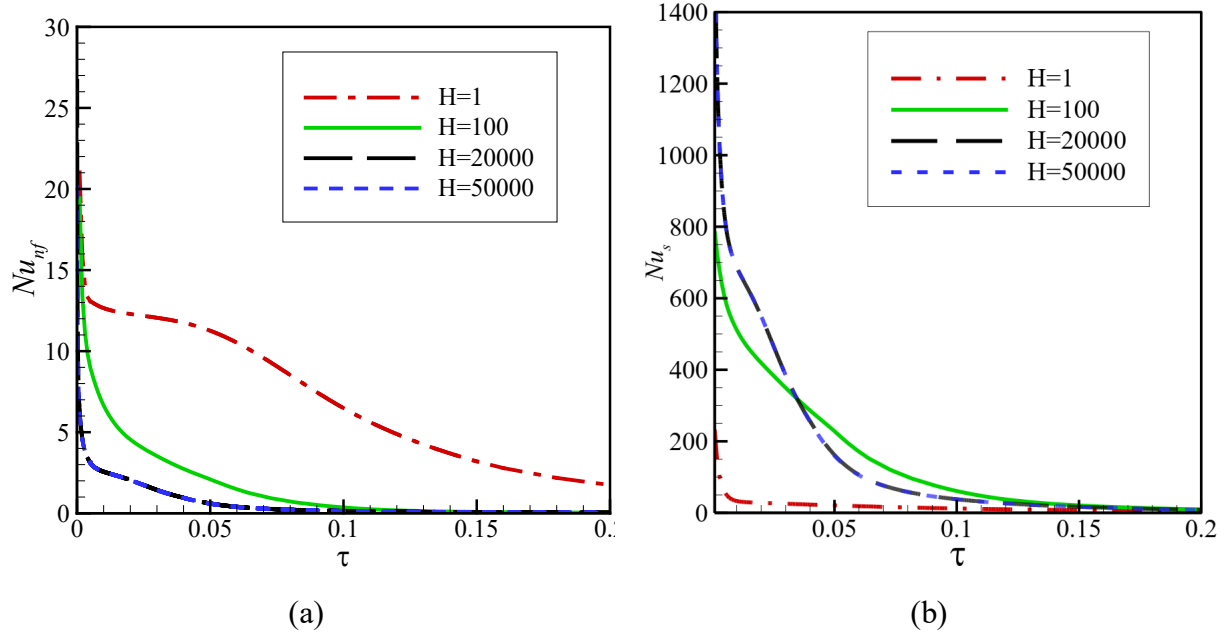
Fig. 12. The effect of various values of interfacial heat transfer coefficient for melting state on (a) Nu_{nf} (b) Nu_s during non-dimensional time when $Da = 10^{-4}$, $R_r = 2.5$, $\lambda = 0.32$, $E_c = -0.75$, $\varepsilon = 0.95$, $\theta_{fu} = 0.5$, $\phi = 0.04$, $Ste = 0.5$, $Pr = 6.2$, and $Ra = 10^7$
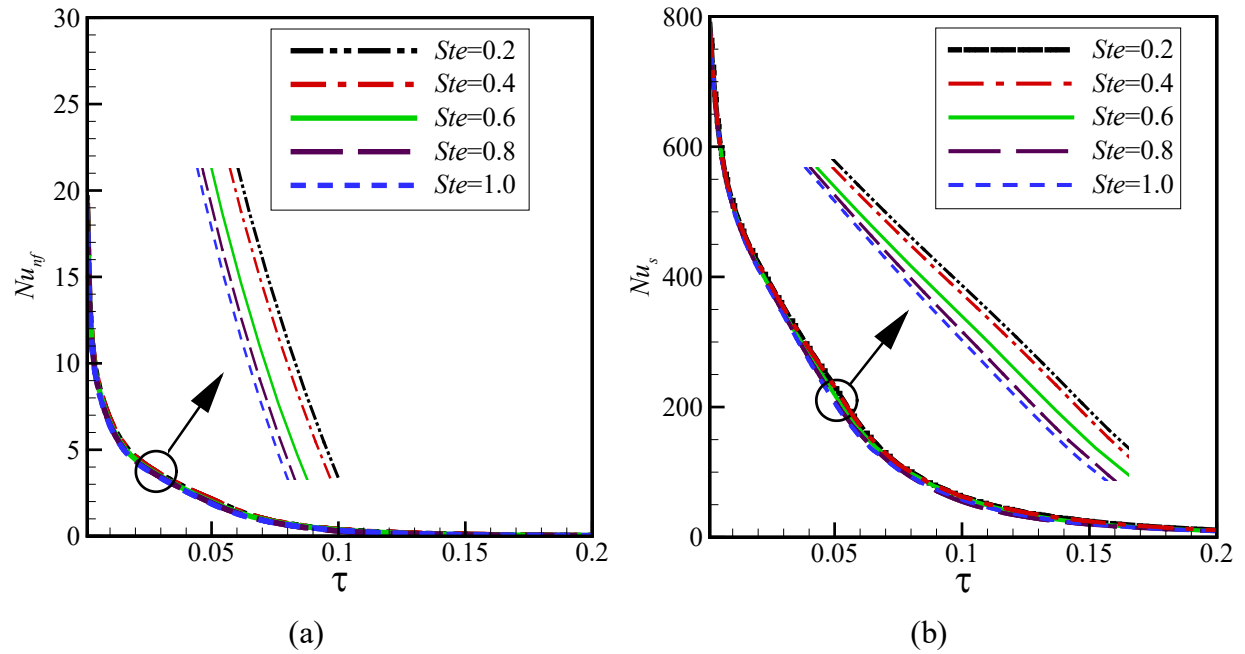

Fig. 13. The effect of various values of Stefan number for melting state on (a) Nu_{nf} (b) Nu_s during non-dimensional time when $Da = 10^{-4}$, $R_r = 2.5$, $\lambda = 0.32$, $E_c = -0.75$, $H = 100$, $\varepsilon = 0.95$, $\theta_{fu} = 0.5$, $\phi = 0.04$, $Pr = 6.2$, and $Ra = 10^7$
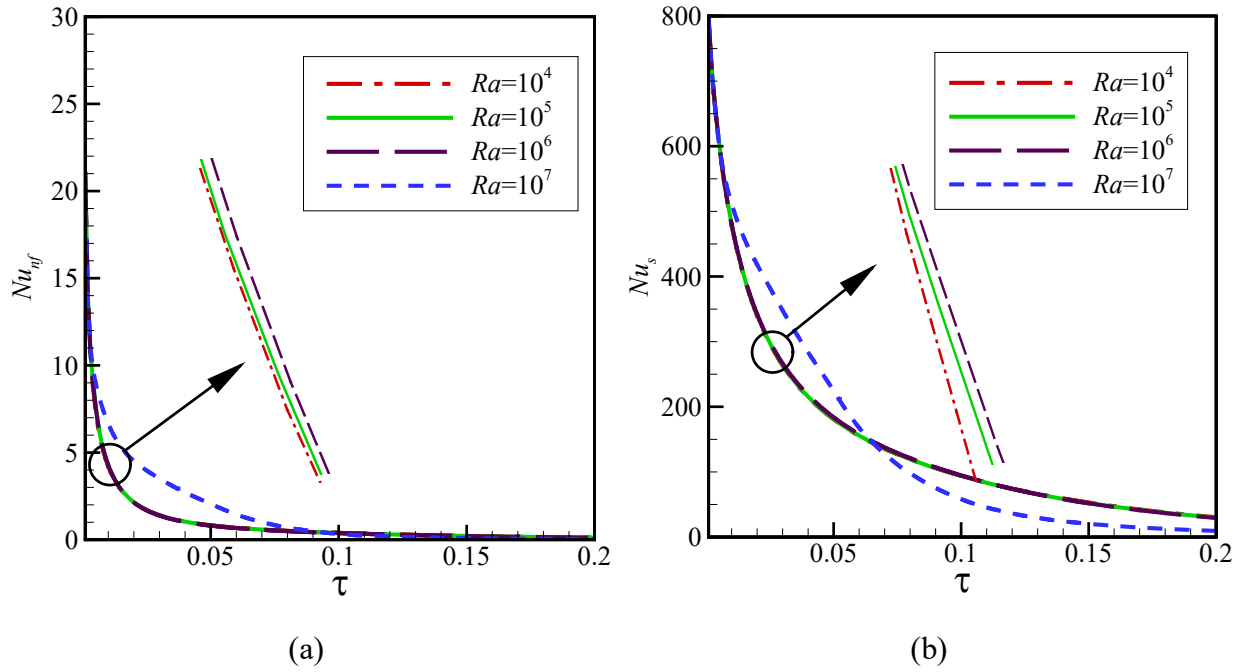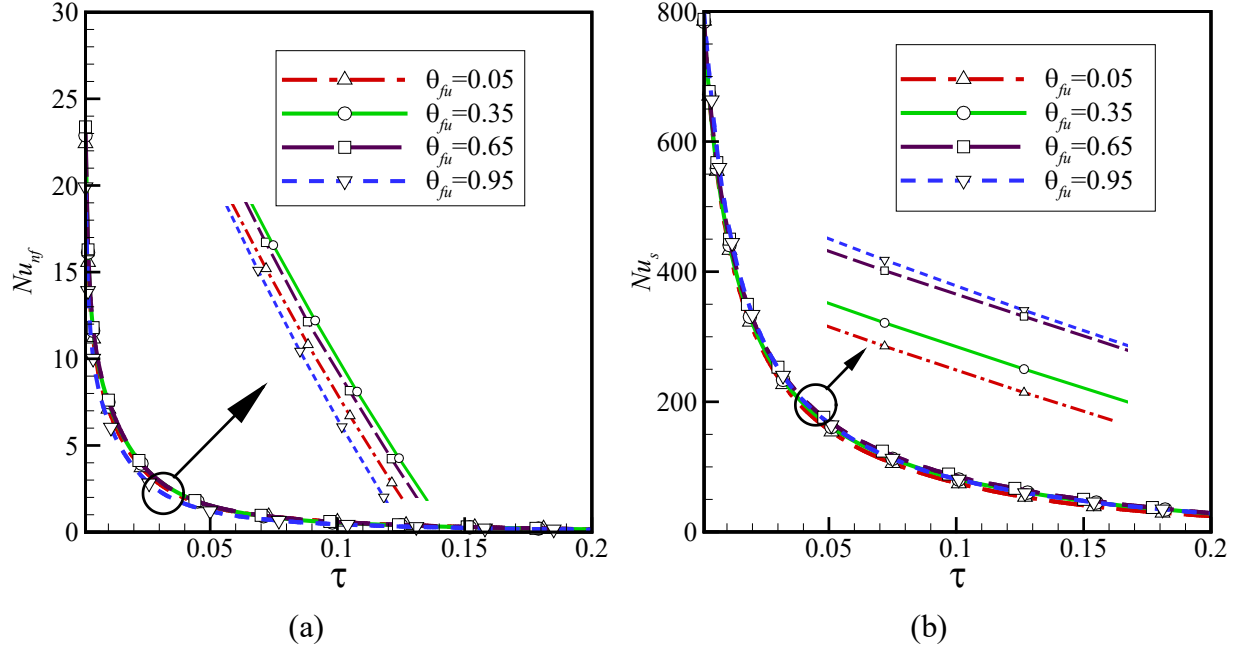
Fig. 14. The effect of selected values of Rayleigh number for melting state on (a) Nu_{nf} (b) Nu_s during non-dimensional time when $Da = 10^{-4}$, $R_r = 2.5$, $\lambda = 0.32$, $E_c = -0.75$, $H = 100$, $\varepsilon = 0.95$, $\theta_{fu} = 0.5$, $\phi = 0.04$, $Ste = 0.5$, and $Pr = 6.2$.
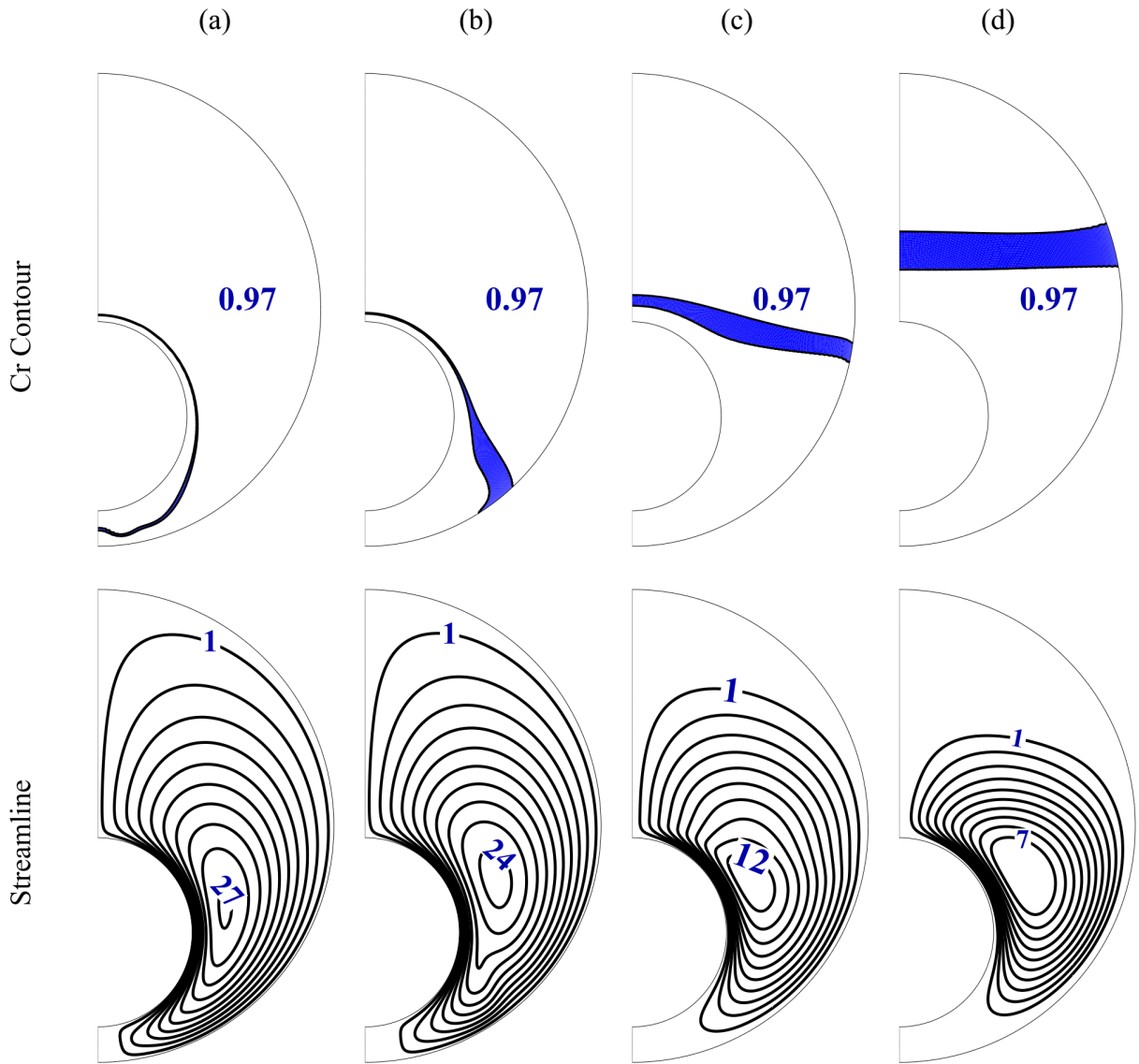
Fig. 15. The snapshots of heat capacity ratio contour and streamlines for solidification state on (a) $\tau = 0.005$, (b) $\tau = 0.01$, (c) $\tau = 0.03$ and (d) $\tau = 0.06$ when $Da = 10^{-4}$, $R_r = 2.5$, $\lambda = 0.32$, $E_c = -0.75$, $H = 100$, $\varepsilon = 0.95$, $\theta_{fu} = 0.5$, $\phi = 0.04$, $Ste = 0.2$, $Pr = 6.2$, and $Ra = 10^7$
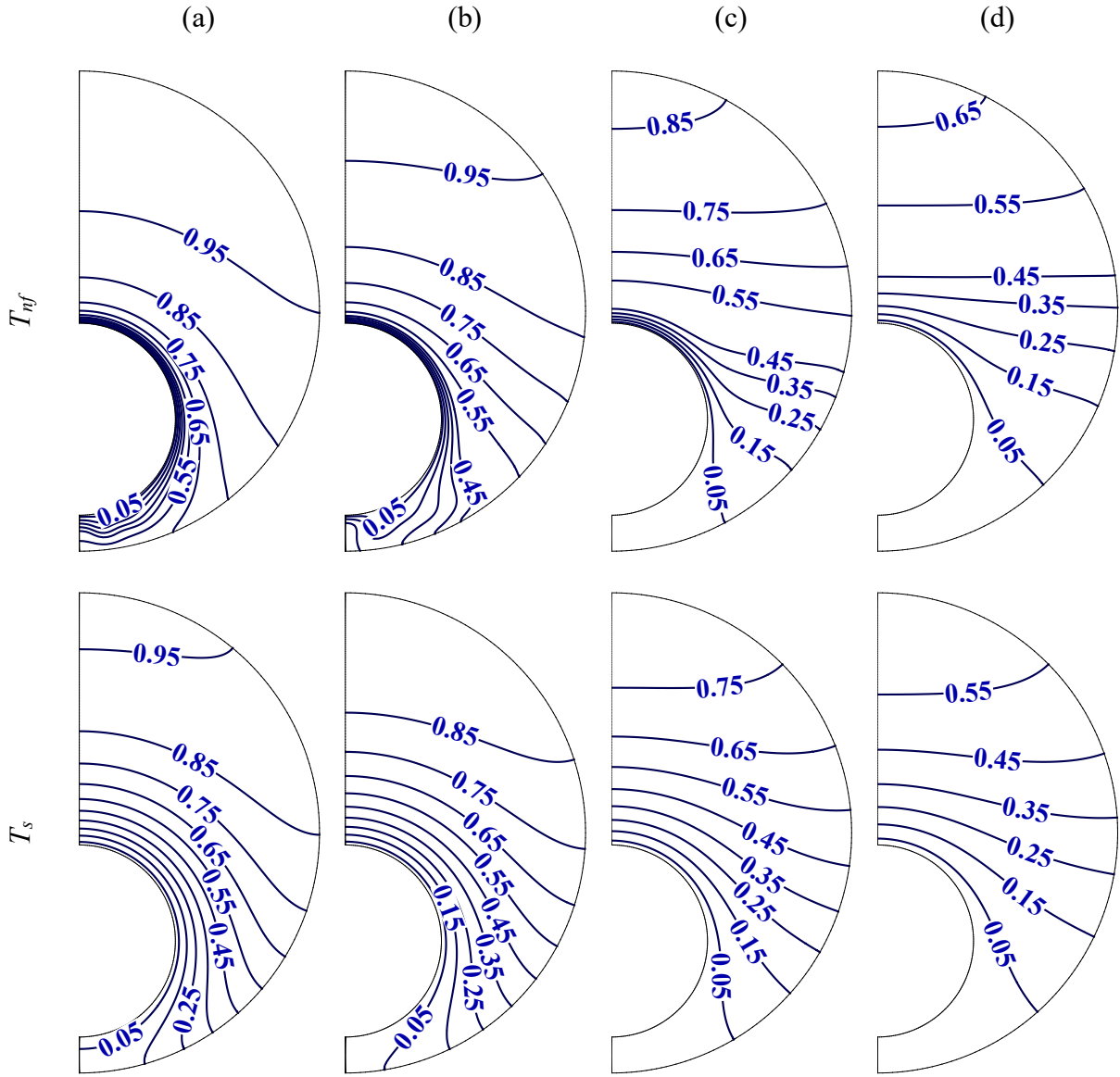
Fig. 16. The Temperature contour of T_{nf} and T_s during times for solidification state on (a) τ = 0.005, (b) τ = 0.01, (c) τ = 0.03 and (d) τ = 0.06 when $Da = 10^{-4}$, $R_r = 2.5$, $\lambda = 0.32$, $E_c = -0.75$, H = 100, $\varepsilon = 0.95$, $\theta_{fu} = 0.5$, $\phi = 0.04$, $Ste = 0.2$, $Pr = 6.2$, and $Ra = 10^7$

Fig. 17. The temporal various dimensionless fusion temperature for solidification state on (a) Nu_{nf} (b) Nu_s when $Da = 10^{-4}$, $R_r = 2.5$, $\lambda = 0.32$, $E_c = -0.75$, $H = 100$, $\varepsilon = 0.95$, $\phi = 0.04$, $Ste = 0.5$, $Pr = 6.2$, and $Ra = 10^7$
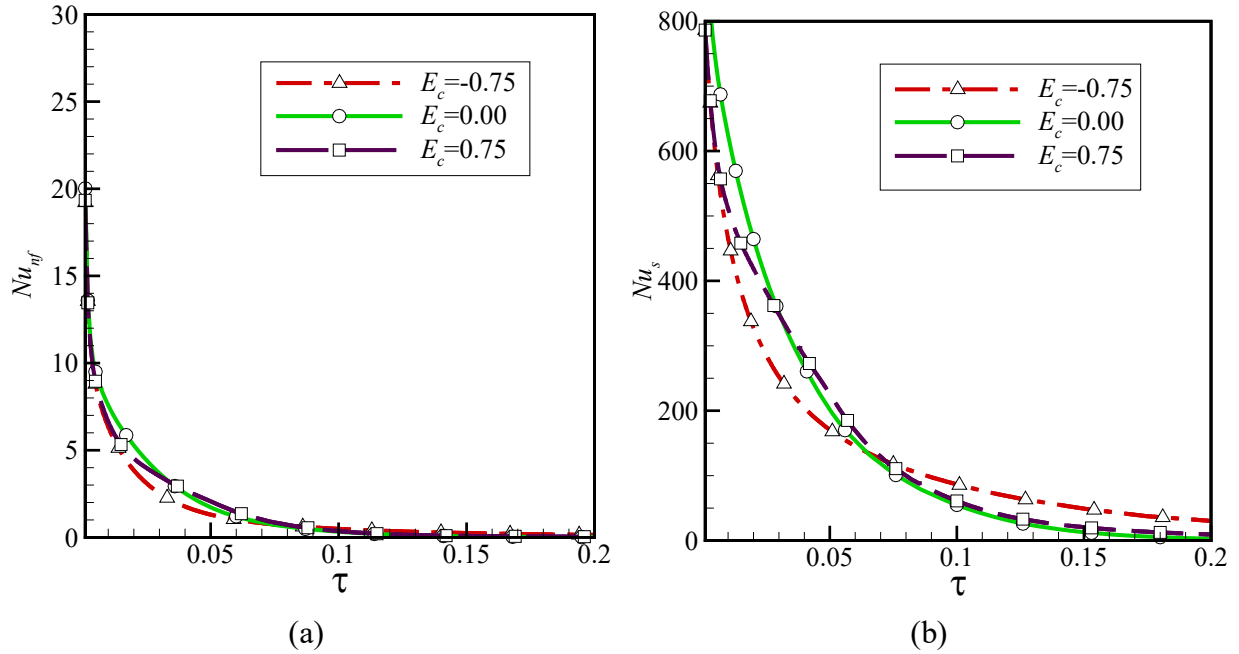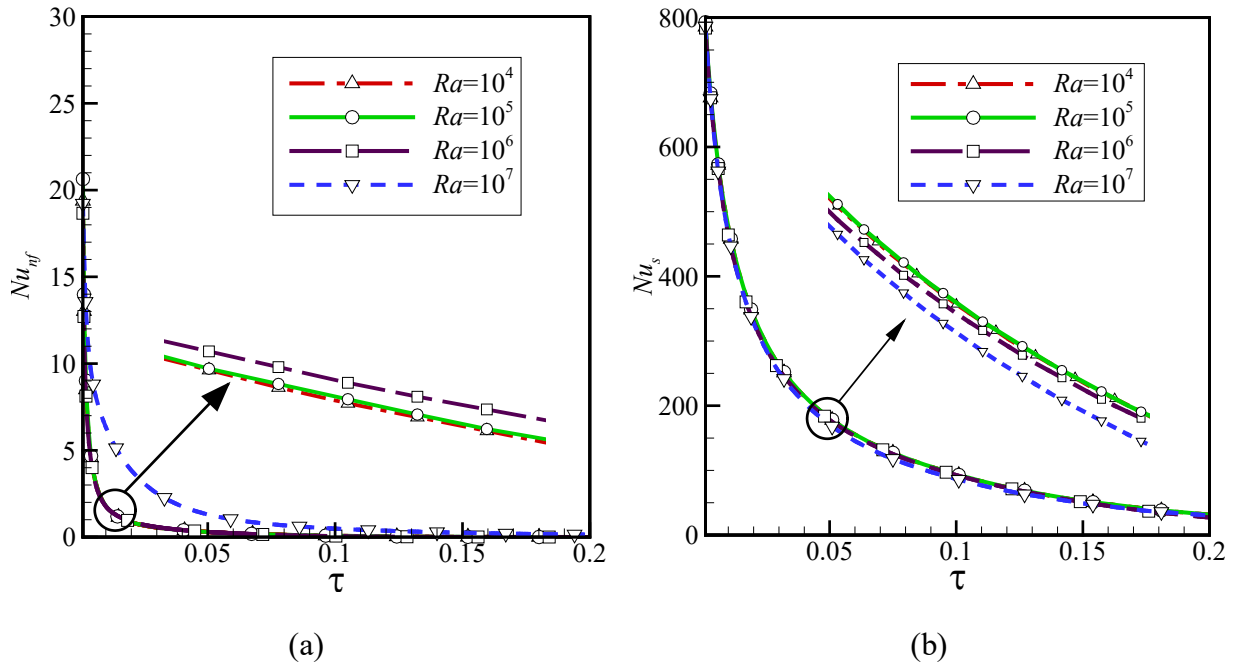

Fig. 18. The effect of various values of eccentricity for solidification state on (a) Nu_{nf} (b) Nu_s during non-dimensional time when $Da = 10^{-4}$, $Ste = 0.5$, $R_r = 2.5$, $\lambda = 0.32$, $H = 100$, $\varepsilon = 0.95$, $\theta_{fu} = 0.5$, $\phi = 0.04$, $Pr = 6.2$, and $Ra = 10^7$
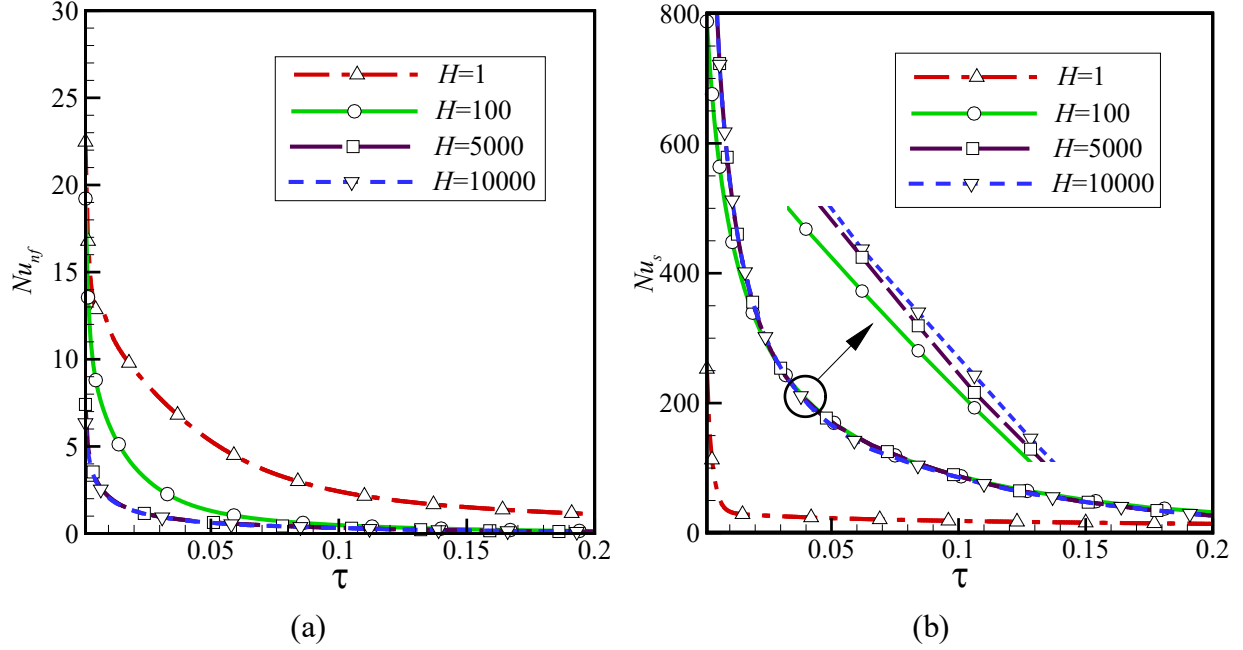
Fig. 19. The effect of various values of interfacial heat transfer coefficient for solidification state on (a) Nu_{nf} (b) Nu_s during non-dimensional time when $Da = 10^{-4}$, $R_r = 2.5$, $\lambda = 0.32$, $E_c = -0.75$, $\varepsilon = 0.95$, $\theta_{fu} = 0.5$, $\phi = 0.04$, $Ste = 0.5$, $Pr = 6.2$, and $Ra = 10^7$
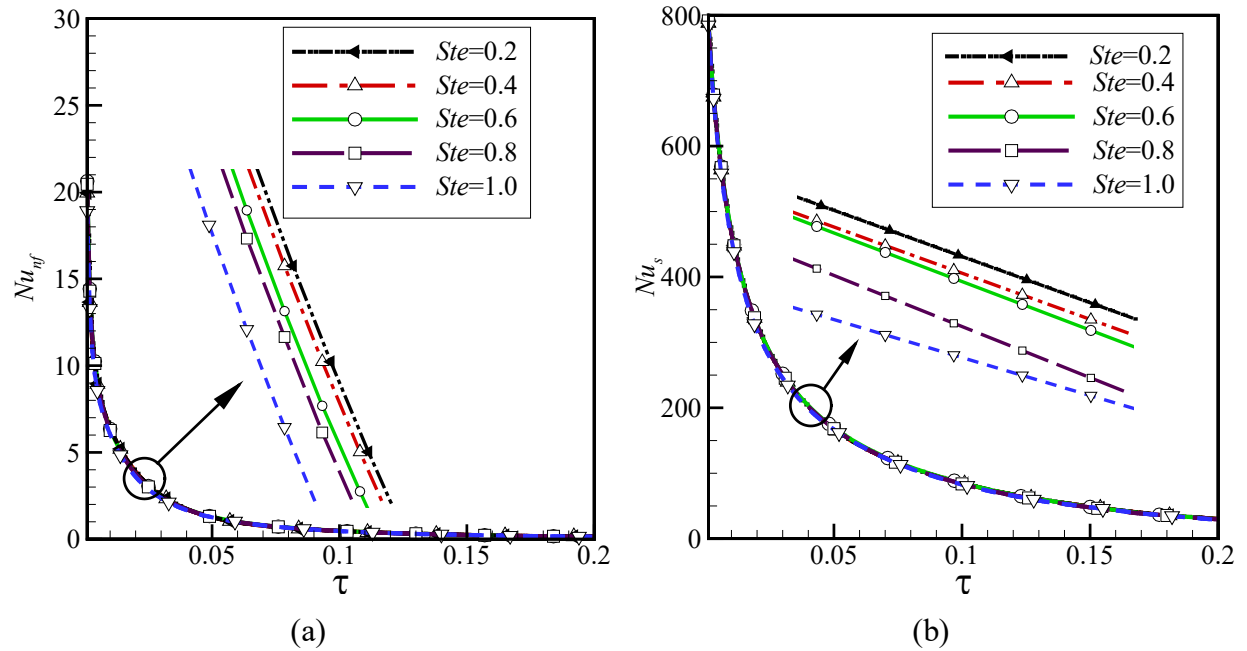
Fig. 20. The effect of various values of Stefan number for solidification state on (a) Nu_{nf} (b) Nu_s during non-dimensional time when $Da = 10^{-4}$, $R_r = 2.5$, $\lambda = 0.32$, $E_c = -0.75$, $H = 100$, $\varepsilon = 0.95$, $\theta_{fu} = 0.5$, $\phi = 0.04$, $Pr = 6.2$, and $Ra = 10^7$

Fig. 21. The effect of various values of Rayleigh number for solidification state on (a) Nu_{nf} (b) Nu_s during non-dimensional time when $Da = 10^{-4}$, $R_r = 2.5$, $\lambda = 0.32$, $E_c = -0.75$, $H = 100$, $\varepsilon = 0.95$, $\theta_{fu} = 0.5$, $\phi = 0.04$, $Ste = 0.5$, and $Pr = 6.2$

References

[1] International Energy Outlook 2019, https://www.eia.gov/outlooks/ieo/.

[2] U. Mikolajewicz, M. Vizcaino, J. Jungclaus, G. Schurgers, Effect of ice sheet interactions in anthropogenic climate change simulations, J Geophysical Research Letters, 34 (2007).

[3] J. Skaalum, D. Groulx, Heat transfer comparison between branching and non-branching fins in a latent heat energy storage system, J International Journal of Thermal Sciences, 152 (2020) 106331.

[4] Z. Wang, J. Wu, D. Lei, H. Liu, J. Li, Z. Wu, Experimental study on latent thermal energy storage system with gradient porosity copper foam for mid-temperature solar energy application, J Applied Energy, 261 (2020) 114472.

[5] A.J. Schrader, H.E. Bush, D. Ranjan, P.G. Loutzenhiser, Aluminum-doped calcium manganite particles for solar thermochemical energy storage: Reactor design, particle characterization, and heat and mass transfer modeling, J International Journal of Heat Mass Transfer, 152 (2020) 119461.

[6] A. Sharma, V.V. Tyagi, C. Chen, D. Buddhi, Review on thermal energy storage with phase change materials and applications, J Renewable Sustainable energy reviews, 13 (2009) 318-345.

[7] P. Singh, R. Sharma, A. Ansu, R. Goyal, A. Sarı, V. Tyagi, A comprehensive review on development of eutectic organic phase change materials and their composites for low and medium range thermal energy storage applications, Solar Energy Materials and Solar Cells, 223 (2021) 110955.

[8] P. Talebizadeh Sardari, G.S. Walker, M. Gillott, D. Grant, D. Giddings, Numerical modelling of phase change material melting process embedded in porous media: effect of heat storage size, Proceedings of the institution of mechanical engineers, Part A: journal of power and energy, 234 (2020) 365-383.

[9] N.S. Bondareva, M.A. Sheremet, Effect of the time-dependent volumetric heat flux on heat transfer performance inside a heat sink based on the phase change materials, Clean Technologies and Environmental Policy, 23 (2021) 1151-1160.

[10] J.M. Mahdi, F.T. Najim, I.M. Aljubury, H.I. Mohammed, N.B. Khedher, N.K. Alshammari, A. Cairns, P. Talebizadehsardari, Intensifying the thermal response of PCM via fin-assisted foam strips in the shell-and-tube heat storage system, Journal of Energy Storage, 45 (2022) 103733.

[11] M. Eisapour, A.H. Eisapour, M. Hosseini, P. Talebizadehsardari, Exergy and energy analysis of wavy tubes photovoltaic-thermal systems using microencapsulated PCM nano-slurry coolant fluid, Applied Energy, 266 (2020) 114849.

[12] K. Ghasemi, S. Tasnim, S. Mahmud, PCM, nano/microencapsulation and slurries: A review of fundamentals, categories, fabrication, numerical models and applications, Sustainable Energy Technologies and Assessments, 52 (2022) 102084.

[13] J.M. Mahdi, H.I. Mohammed, E.T. Hashim, P. Talebizadehsardari, E.C. Nsofor, Solidification enhancement with multiple PCMs, cascaded metal foam and nanoparticles in the shell-and-tube energy storage system, Applied Energy, 257 (2020) 113993.

[14] N. Alsedais, A.M. Aly, Double-diffusive convection from an oscillating baffle embedded in an astroid-shaped cavity suspended by nano encapsulated phage change materials: ISPH simulations, Waves in Random and Complex Media, (2021) 1-20.

[15] A.M. Aly, A. Al-Hanaya, Z. Raizah, The magnetic power on natural convection of NEPCM suspended in a porous annulus between a hexagonal-shaped cavity and dual curves, Case Studies in Thermal Engineering, 28 (2021) 101354.

[16] F.H. Ali, H.K. Hamzah, A.K. Hussein, M.Y. Jabbar, P. Talebizadehsardari, MHD mixed convection due to a rotating circular cylinder in a trapezoidal enclosure filled with a nanofluid saturated with a porous media, International Journal of Mechanical Sciences, 181 (2020) 105688.

[17] A. Shahsavar, M. Rashidi, M.M. Mosghani, D. Toghraie, P. Talebizadehsardari, A numerical investigation on the influence of nanoadditive shape on the natural convection and entropy generation inside a rectangle-shaped finned concentric annulus filled with boehmite alumina nanofluid using two-phase mixture model, Journal of Thermal Analysis and Calorimetry, 141 (2020) 915-930.

[18] M.K. Nayak, F. Mabood, A. Dogonchi, K.M. Ramadan, I. Tlili, W.A. Khan, Entropy optimized assisting and opposing non-linear radiative flow of hybrid nanofluid, Waves in Random and Complex Media, (2022) 1-22.

[19] M. Sheikholeslami, M. Ijaz Khan, Y.M. Chu, S. Kadry, W.A. Khan, CVFEM based numerical investigation and mathematical modeling of surface dependent magnetized copper-oxide nanofluid flow using new model of porous space, Numerical Methods for Partial Differential Equations.

[20] M. Bechiri, K. Mansouri, Analytical study of heat generation effects on melting and solidification of nano-enhanced PCM inside a horizontal cylindrical enclosure, J Applied Thermal Engineering, 104 (2016) 779-790.

[21] S.T. Latibari, M. Mehrali, M. Mehrali, T.M.I. Mahlia, H.S.C. Metselaar, Synthesis, characterization and thermal properties of nanoencapsulated phase change materials via sol–gel method, J Energy, 61 (2013) 664-672.

[22] M. Jourabian, M. Farhadi, Technology, Melting of nanoparticles-enhanced phase change material (NEPCM) in vertical semicircle enclosure: numerical study, J Journal of Mechanical Science, 29 (2015) 3819-3830.

[23] A. Alsabery, M. Sheremet, M. Sheikholeslami, A. Chamkha, I. Hashim, Magnetohydrodynamics energy transport inside a double lid-driven wavy-walled chamber: Impacts of inner solid cylinder and two-phase nanoliquid approach, International Journal of Mechanical Sciences, 184 (2020) 105846.

[24] P.M. Patil, H.F. Shankar, M.A. Sheremet, Influence of Liquid Hydrogen Diffusion on Nonlinear Mixed Convective Circulation around a Yawed Cylinder, Symmetry, 14 (2022) 337.

[25] S. Barlak, O.N. Sara, A. Karaipekli, S. Yapıcı, Thermal conductivity and viscosity of nanofluids having nanoencapsulated phase change material, Nanoscale and Microscale Thermophysical Engineering, 20 (2016) 85-96.

[26] L. Chai, R. Shaukat, L. Wang, H.S. Wang, A review on heat transfer and hydrodynamic characteristics of nano/microencapsulated phase change slurry (N/MPCS) in mini/microchannel heat sinks, Applied Thermal Engineering, 135 (2018) 334-349.

[27] M. Ghalambaz, A.J. Chamkha, D. Wen, Natural convective flow and heat transfer of Nano-Encapsulated Phase Change Materials (NEPCMs) in a cavity, International Journal of Heat and Mass Transfer, 138 (2019) 738-749.

[28] B. Chen, X. Wang, R. Zeng, Y. Zhang, X. Wang, J. Niu, Y. Li, H. Di, An experimental study of convective heat transfer with microencapsulated phase change material suspension: laminar flow in a circular tube under constant heat flux, Experimental Thermal and Fluid Science, 32 (2008) 1638-1646.

[29] K. Khanafer, K. Vafai, A critical synthesis of thermophysical characteristics of nanofluids, International journal of heat and mass transfer, 54 (2011) 4410-4428.

[30] H.R. Seyf, Z. Zhou, H. Ma, Y. Zhang, Three dimensional numerical study of heat-transfer enhancement by nano-encapsulated phase change material slurry in microtube heat sinks with tangential impingement, International journal of heat and mass transfer, 56 (2013) 561-573.

[31] A.C. Baytas, I. Pop, Free convection in a square porous cavity using a thermal nonequilibrium model, International Journal of Thermal Sciences, 41 (2002) 861-870.

[32] K. Kahveci, Buoyancy driven heat transfer of nanofluids in a tilted enclosure, Journal of Heat Transfer, 132 (2010).

[33] M. Kanashina, P. Zubkov, E.V. Kalabin, NATURAL CONVECTIVE HEAT TRANSFER IN A SQUARE CAVITY WITH TIME-VARYING SIDEWALL TEMPERATURE, in: CHT-04-Advances in Computational Heat Transfer III. Proceedings of the Third International Symposium, Begel House Inc., 2004.

[34] T. Kuehn, R. Goldstein, An experimental and theoretical study of natural convection in the annulus between horizontal concentric cylinders, Journal of Fluid mechanics, 74 (1976) 695-719.

[35] E.V. Kalabin, M.V. Kanashina, P.T. Zubkov, NATURAL-CONVECTIVE HEAT TRANSFER IN A SQUARE CAVITY WITH TIME-VARYING SIDE-WALL TEMPERATURE, Numerical Heat Transfer, Part A: Applications, 47 (2005) 621-631.